Sun-to-Earth MHD Simulation of the 2000 July 14 "Bastille Day" Eruption

Tibor Török , Cooper Downs , Jon A. Linker, R. Lionello , Viacheslav S. Titov , Zoran Mikić , Pete Riley,
Ronald M. Caplan , and Janvier Wijaya
Predictive Science Inc., 9990 Mesa Rim Road, Suite 170, San Diego, CA 92121, USA; tibor@predsci.com

Abstract

Solar eruptions are the main driver of space-weather disturbances at Earth. Extreme events are of particular interest, not only because of the scientific challenges they pose, but also because of their possible societal consequences. Here we present a magnetohydrodynamic (MHD) simulation of the 2000 July 14 "Bastille Day" eruption, which produced a very strong geomagnetic storm. After constructing a "thermodynamic" MHD model of the corona and solar wind, we insert a magnetically stable flux rope along the polarity inversion line of the eruption's source region and initiate the eruption by boundary flows. More than 10^{33} erg of magnetic energy is released in the eruption within a few minutes, driving a flare, an extreme-ultraviolet wave, and a coronal mass ejection (CME) that travels in the outer corona at ≈ 1500 km s^{-1}, close to the observed speed. We then propagate the CME to Earth, using a heliospheric MHD code. Our simulation thus provides the opportunity to test how well in situ observations of extreme events are matched if the eruption is initiated from a stable magnetic equilibrium state. We find that the flux-rope center is very similar in character to the observed magnetic cloud, but arrives ≈ 8.5 hr later and $\approx 15°$ too far to the north, with field strengths that are too weak by a factor of ≈ 1.6. The front of the flux rope is highly distorted, exhibiting localized magnetic field concentrations as it passes 1 au. We discuss these properties with regard to the development of space-weather predictions based on MHD simulations of solar eruptions.

Key words: magnetohydrodynamics (MHD) – Sun: corona – Sun: coronal mass ejections (CMEs)

1. Introduction

Coronal mass ejections (CMEs) are immense eruptions that propel plasma and magnetic flux outward from the Sun. CMEs (and accompanying solar flares) are the largest impulsive energy-release events in the solar system and are therefore of inherent scientific interest. There are many open scientific questions about such events, such as, how is the energy released so impulsively, and how are CMEs initiated?

The strongest solar eruptions are typically characterized by very fast (>1000 km s^{-1}) CMEs and X-class solar flares, such as the famous "Bastille Day" event considered in this article. Such "extreme" eruptions are responsible for the most severe space-weather effects at Earth. Fast CMEs are the primary cause of major geomagnetic storms and are typically associated with solar energetic particle events (e.g., Gopalswamy 2006), both of which can represent a significant hazard for humans and technological infrastructure (e.g., Baker & Lanzerotti 2016).

Particles accelerated during a flare or CME can reach the Earth within half an hour or less (e.g., Schwadron et al. 2014), leaving little time for a quantitative prediction of their consequences. On the other hand, even the fastest CMEs require almost a day to arrive at Earth and initiate a geomagnetic storm. This provides, in principle, sufficient time to predict their impact. The geoeffectiveness of CMEs, that is, of the associated interplanetary CME (ICME) or magnetic cloud (MC), depends primarily on their Earth-side magnetic field direction (B_z), their velocity, and their associated ram pressure upon arrival at the magnetosphere (e.g., Srivastava & Venkatakrishnan 2004; Gopalswamy et al. 2008). It is therefore highly desirable to predict these parameters before an ICME (and the shock that potentially precedes it) arrives at Earth (e.g., Siscoe & Schwenn 2006; Messerotti et al. 2009). A candidate tool for this purpose is magnetohydrodynamic (MHD) numerical simulations.

MHD simulations have been widely employed to model CMEs. Many of them use idealized configurations and are primarily intended to investigate specific aspects of CMEs, such as their initiation mechanisms (e.g., Forbes 1990; Mikić & Linker 1994; Amari et al. 1996, 2000, 2003; Antiochos et al. 1999; Chen & Shibata 2000; Fan & Gibson 2003; Kusano et al. 2004, 2012; Lynch et al. 2005; Török & Kliem 2005, 2007; Aulanier et al. 2010; Karpen et al. 2012). For reviews on such simulations and the underlying theoretical concepts, see, for example, Forbes et al. (2006), Chen (2011), Aulanier (2014), and Green et al. (2018).

Other simulations are specifically designed to model observed events. They typically derive boundary conditions for the magnetic field from observed magnetograms and produce the pre-eruptive configuration using boundary flows, nonlinear force-free field (NLFFF) extrapolations, or analytical flux-rope models that are inserted into the source region of the eruption. Some of these simulations just model the initiation and coronal evolution of CMEs (e.g., Lugaz et al. 2007, 2009; Roussev et al. 2007; Cohen et al. 2009; Zuccarello et al. 2012; Kliem et al. 2013; Amari et al. 2014, 2018; Fan 2016; Jiang et al. 2016), while others include the propagation of the associated ICME to one astronomical unit (au) or beyond (e.g., Manchester et al. 2004; Tóth et al. 2007; Shen et al. 2014). In some cases, the modeling of the eruption is fully neglected, and simplified initial conditions for the CME or ICME (sometimes merely a velocity perturbation) are set up at some distance from the Sun in the corona or in the inner heliosphere (e.g., Odstrcil et al. 2005; Shen et al. 2014; Zhou et al. 2014; Shiota & Kataoka 2016).

At the present time, the most advanced simulations of observed eruptions additionally use a sophisticated treatment of the energy transfer in the corona that includes thermal conduction, radiative losses, and empirical (or wave-turbulence driven) coronal heating, which is often referred to as

"thermodynamic MHD" (Linker et al. 2001; Lionello et al. 2001, 2009; Downs et al. 2010, 2013; van der Holst et al. 2010, 2014; Sokolov et al. 2013). This description is required for modeling the plasma properties in the corona to a degree of realism that allows one to produce synthetic satellite images that can be directly compared to observations (Lionello et al. 2009). CMEs are then launched in this background environment in the source region of the eruption (e.g., Downs et al. 2011, 2012; Lugaz et al. 2011; Manchester et al. 2012; Jin et al. 2013, 2016) and sometimes coupled to a simpler heliospheric MHD model to propagate the associated ICME to 1 au or beyond (e.g., Lionello et al. 2013; Manchester et al. 2014; Merkin et al. 2016; Jin et al. 2017a).

Thermodynamic MHD simulations are complex and computationally expensive and have therefore not yet been used for operational space-weather predictions, even when coupled to computationally more efficient heliospheric simulations. At present, the only three-dimensional MHD model that is used for operational forecasts (at the NOAA Space Weather Prediction Center) is the WSA-ENLIL model (e.g., Odstrcil et al. 2005). ICMEs (with no magnetic field of their own) are simulated in this model by specifying a cone of constant velocity at the inner boundary of a heliospheric domain. In the foreseeable future, however, the steadily increasing computational capabilities may allow the use of thermodynamic MHD simulations for real-time space-weather predictions (Jin et al. 2017b). It is thus important to continuously improve the capabilities and accuracy of these simulations.

Here we describe a coupled thermodynamic–heliospheric MHD simulation of the 2000 July 14 Bastille Day solar eruption. The simulation covers the evolution of the event from its pre-eruptive state low in the corona to the arrival of the ICME at 1 au. The Bastille Day event was one of the strongest eruptions of solar cycle 23 (see Section 2); it thus provides an excellent case for testing the ability of MHD simulations to reproduce the observed properties of extreme eruptions.

An important feature of our simulation is the construction of a pre-eruptive configuration that is in stable magnetic equilibrium. This extends other thermodynamic MHD simulations of observed eruptions, which typically insert a magnetic flux rope that is not in magnetic equilibrium into the background corona to initiate a CME (e.g., Manchester et al. 2008; Lugaz et al. 2011; Jin et al. 2017a). This "out-of-equilibrium" approach is technically convenient, as it reduces the complexity of the computation while reproducing many observed CME/ICME properties sufficiently well. It is, therefore, a reasonable approach for trying to develop operational space-weather forecasts via MHD simulations in the near future. However, in the longer term, a physically better constrained modeling of CMEs, starting from a stable magnetic equilibrium, is preferable from both a forecasting and a scientific perspective, for several reasons.

First, large-scale solar eruptions always originate from stable configurations, so any realistic model should aim to reproduce this property. Second, it is an open question how the free magnetic energy necessary to power eruptions, especially extreme events, can be stored in the corona and subsequently be released on a rapid timescale. This can only be investigated with models that use equilibrium configurations, while out-of-equilibrium models may release significantly more energy than is actually available. Third, starting from stable equilibrium configurations allows one to (1) directly compare and constrain

the model with observations of the pre-eruptive source region, (2) apply and test different physical mechanisms for the triggering of CMEs, (3) include the slow rise phase that precedes many eruptions (e.g., Liu et al. 2012), (4) model cases in which the eruption proceeds successively along the polarity inversion line (PIL; e.g., Liu et al. 2009; see also Sections 3.2–3.3), and (5) simulate the early kinematic and dynamic evolution of CMEs, as well as phenomena associated with this early phase (e.g., shock formation low in the corona, extreme ultraviolet (EUV) waves, dimmings) in a more realistic manner (e.g., Downs et al. 2011). Specifically, out-of-equilibrium flux ropes, due to their immediate expansion, may not be well suited for modeling the frequently observed, B_z-relevant rotation of CMEs about their rise direction (e.g., Démoulin 2008; Thompson et al. 2012), especially in cases where most of the rotation occurs low in the corona, while the ejected flux is still accelerating (e.g., Török et al. 2010; Kliem et al. 2012; Fan 2016). Furthermore, inserting a flux rope into a background corona inevitably triggers an unphysical, wave-like perturbation of the system, which superimposes with the modeled CME if the latter starts immediately. While such a perturbation may be damped to some degree by adding sufficient mass to the rope, it is preferable to let it propagate away from the source region before a CME is initiated.

Finally, MHD simulations that aim to reproduce (or predict) in situ measurements of ICMEs presently rely on observations of the associated eruption. Typically, the propagation speed of the CME in the corona is required, in order to impose an appropriate velocity perturbation on the system (e.g., Odstrcil et al. 2005; Shen et al. 2014) or to constrain initial flux-rope parameters (Jin et al. 2017b). In contrast, simulations that start from a stable pre-eruptive configuration produce CME properties such as the field strength, orientation, and speed self-consistently, so no observations of the actual eruption are required to set up the simulation.[1] This allows one to predict the properties and impact of a potential eruption *before* it has occurred, and it provides the means to assess the strength and impact of eruptions that a given source region on the Sun may produce.

A concise overview of our simulation was given in Linker et al. (2016); here we present a more extended description of the numerical setup, the methodology, and the results. This article is organized as follows. In Section 2, we briefly describe the Bastille Day event and the associated ICME. In Section 3, we present our numerical setup and methodology, with particular focus on the construction of the pre-eruptive configuration. In Section 4, we describe the eruption, discuss the conditions necessary for storing adequate magnetic energy to power such extreme events, and compare the simulation with the observation. Section 5 addresses the results of our heliospheric simulation and their comparison with in situ data. We conclude with a summary and discussion in Section 6.

2. The Bastille Day Event

The Bastille Day eruption occurred on 2000 July 14 in active region (AR) NOAA 9077. It was one of the largest events during solar cycle 23. The event has been studied extensively, and many articles have been published, including a special

---

[1] In the case presented here, we used the observed flare arcade to constrain the initial flux-rope configuration (Sections 3.2–3.3). However, such simulations can be set up by using only *pre-eruptive* observations such as the location of filaments, sigmoids, or shear along the PIL obtained from vector data.

volume of Solar Physics (2001, Vol. 204, Issue 1–2). At the onset of the eruption, the AR was located at the disk center, about 15°–20° north of the equator. The event consisted of a filament eruption, an X5.7 flare starting at 10:03 UT, and a fast halo CME with a propagation speed of up to about 1700 km s^{-1} (Andrews 2001). The flare was followed by an intense radiation storm that resulted in one of the 16 ground-level enhancement events of cycle 23 (Bieber et al. 2002). The shock wave driven by the ICME associated with the eruption reached the *WIND* spacecraft (Lepping et al. 1995; Lin et al. 1995) and the *Advanced Composition Explorer* (*ACE*; Stone et al. 1998) in ≈28 hr, followed by a large MC that arrived ≈5 hr later, around 19 UT on July 15, with a field strength of ≈50 nT and a speed of ≈1100 km s^{-1} (e.g., Smith et al. 2001). The MC, carrying a strong southward magnetic field component ("negative B_z"), produced a very strong geomagnetic storm with a minimum geomagnetic storm index, *Dst*, lower than −300 nT (Lepping et al. 2001). The in situ magnetic-field measurements taken at *ACE* suggest that the spacecraft passed below the axis of a left-handed flux rope (Yurchyshyn et al. 2001).

The Bastille Day event was followed ≈3.5 hr later by a second, weaker eruption that occurred at the western edge of the AR and produced an M3.7 flare (e.g., Andrews 2001). This second eruption occurs self-consistently in our simulation, without the need to impose boundary driving or some other external perturbation to initiate it. This suggests that these two eruptions were "sympathetic" events (e.g., Schrijver & Title 2011; Török et al. 2011; see Section 4.5 for details).

We note that the time period around the Bastille Day event was characterized by strong eruptive activity. For example, a large transequatorial filament, apparently connected to the eastern section of NOAA AR 9077, erupted almost simultaneously (Wang et al. 2006). Moreover, several ICMEs and shocks associated with eruptions were observed by *ACE* and *WIND* in the 5 to 6 days before the MC associated with the Bastille Day CME arrived at Earth (e.g., Smith et al. 2001; Wang et al. 2001; Richardson & Cane 2010). None of these additional eruptions is included in our simulation. Yet, since they potentially influenced the evolution, trajectory, and final state at 1 au of the Bastille Day event in unknown ways, their presence has to be taken into account when evaluating the accuracy of our simulation (see Section 6).

3. Numerical Setup and Methodology

The coronal evolution of the Bastille Day event (Section 4) was modeled using the thermodynamic MHD code "Magneto-hydrodynamic Algorithm outside a Sphere" (MAS), developed and maintained at Predictive Science Inc. (see Appendix A for details). The interplanetary propagation of the associated ICME to Earth (5) was modeled using the recently updated heliospheric capabilities of the MAS code (Lionello et al. 2013). In this section, we summarize our methodology and the numerical setups for the two simulations, paying particular attention to the description of the steps that were used to produce a magnetically stable pre-eruptive configuration.

3.1. Global Coronal Background Configuration

To provide a realistic background environment for the eruption and the associated CME, we first develop a thermodynamic MHD model of the global corona. To calculate
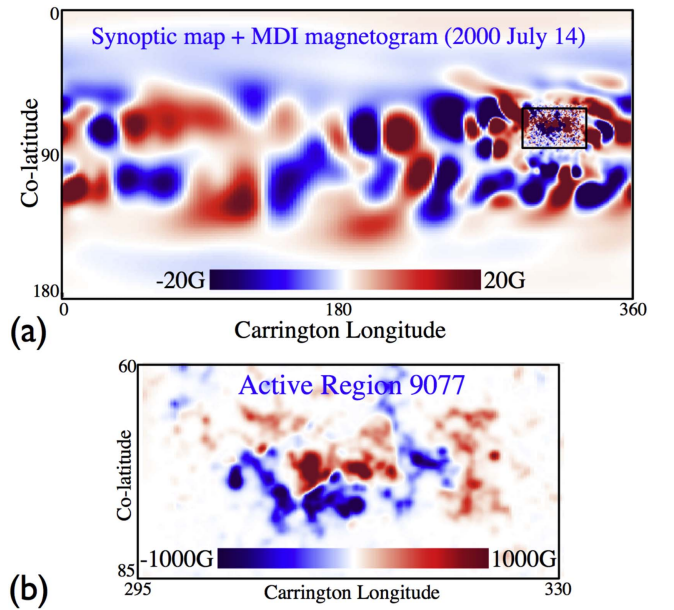

Figure 1. Magnetic map of the radial magnetic field, B_r, at the solar surface, used as boundary condition in the coronal simulation. (a) Full surface field, derived from an MDI synoptic map and an MDI full-disk magnetogram (see text for details). (b) Close-up view of AR NOAA 9077 (outlined by the small box in (a)), where the Bastille Day event and a successive second eruption originated. The maximum magnitude of B_r is 1986 G.

a potential magnetic field that serves as the initial condition for the model, we have to specify the radial field component, B_r, at the boundary $r = R_\odot$, where $R_\odot$ is the solar radius. To this end, we combine a line-of-sight (LOS) *Solar and Heliospheric Observatory* (*SOHO*) Michelson Doppler Imager (MDI; Scherrer et al. 1995) synoptic map for Carrington rotation 1965 (2000 July 10 to August 6) with an LOS MDI magnetogram measured on 2000 July 14 at 09:35 UT, about half an hour prior to the flare onset (Figure 1). To retain as much structure as possible, most of the cells of the numerical grid are concentrated in NOAA AR 9077. Outside the AR, where the grid begins to coarsen, we smooth the synoptic-map magnetic data corresponding to the resolution of the grid. The areas around the poles, where no measurements exist or are not reliable, are fitted in the synoptic map using extrapolation techniques as described in Linker et al. (2013).

A particular challenge for the modeling of extreme eruptions is to construct a pre-eruptive configuration that, on one hand, obeys the observational constraints and, on the other hand, contains a sufficiently large amount of free magnetic energy to reproduce the observed impulsiveness of the eruption and the speed of the associated CME. As demonstrated by Mikić et al. (2013a), a prerequisite for achieving this goal is to avoid oversmoothing (or overdiffusing) the observed magnetogram of the source region. Inside the AR, we thus use a flux-preserving method to resample the LOS MDI magnetogram to a Carrington map with an angular resolution of ≈0.2° (about the width of 2 MDI pixels). This produces a smooth but still high-resolution magnetic field when interpolated onto our numerical mesh (≈0.1°).

The coronal solution is calculated on a nonuniform spherical (r, θ, ϕ) mesh that ranges from 1 $R_\odot$ (the solar surface) to 20 $R_\odot$ (beyond the sonic and Alfvénic critical points). We choose a resolution of 401 × 351 × 471 mesh points, with Δr

in the range $4.5 \times 10^{-4} R_\odot$ (in the transition region) to $0.4 R_\odot$ (at the outer boundary), and latitudinal/longitudinal cells of ≈ 0.0017–0.0019 radians in the area of NOAA AR 9077. The temperature and number density at the lower boundary are fixed to 2×10^4 K and 2×10^{12} cm^{-3}, respectively, similar to the upper chromosphere (see Appendix A). The coronal heating function is specified empirically, in a manner similar to that in Lionello et al. (2009) and Downs et al. (2013). The parameterization is chosen to give a reasonable match to the observed EUV and soft X-ray emission. The thermodynamic MHD model is calculated for 160 Alfvén times, corresponding to about 64 hr ($1 \tau_A \approx 24$ minutes), until the solar wind has fully opened up the field associated with coronal holes, resulting in a steady-state MHD solution.

Figure 2 provides some impressions of the resulting configuration. Panel (a) shows open field lines associated with coronal holes, together with hotter field lines in closed-field areas. Several streamers, visualized by electric currents, can be seen. Panels (b) and (c) show, respectively, the pre-eruptive corona as observed by the Extreme Ultraviolet Imaging Telescope (EIT; Delaboudinière et al. 1995) on board *SOHO* and the Soft X-ray Telescope (SXT; Tsuneta et al. 1991) on board *Yohkoh*, together with synthetic emission images in the same or similar passbands obtained from the simulation. One can see that, while observed features such as coronal holes are partly reproduced in the simulation, the overall complexity outside NOAA AR 9077 is removed. This is because we concentrated the majority of available mesh points in the AR.

3.2. Active-region Energization

After the MHD relaxation of the global corona, the magnetic field in the core of NOAA AR 9077 is still relatively close to a potential field (see the left panel in Figure 4(d)). To model an eruption, the AR has to be energized. As discussed in the Introduction, an important aspect of our approach is modeling an eruption starting from a configuration in stable magnetic equilibrium. In this subsection, we describe the overall energization procedure (Section 3.2.1), the construction of the pre-eruptive flux rope (Section 3.2.2), and the changes resulting from the insertion of the flux rope into the global configuration (Section 3.2.3).

3.2.1. Overall Procedure

To energize the AR, we first construct a magnetic flux rope along the eruptive section of the AR's PIL and then insert it into the global thermodynamic MHD solution. A simple superposition of a (line-tied) flux rope with the magnetic field of the global solution would introduce a significant change of the observed magnetogram that we used to produce that field. To avoid such an unphysical perturbation of the system, we employ a technique that allows us to insert the flux rope such that the original magnetogram is preserved. Our technique is similar to the one used in the "flux rope insertion method" (van Ballegooijen 2004).

In practice, we separately develop our pre-eruptive flux-rope configuration with the same surface B_r distribution (B_{r0}) as the full coronal model (see below). To preserve B_{r0}, we first calculate the desired flux-rope configuration and compute the photospheric B_r associated with this solution. We then subtract the new B_r distribution from the original B_{r0} and obtain a new potential field. We finally insert the flux rope into this
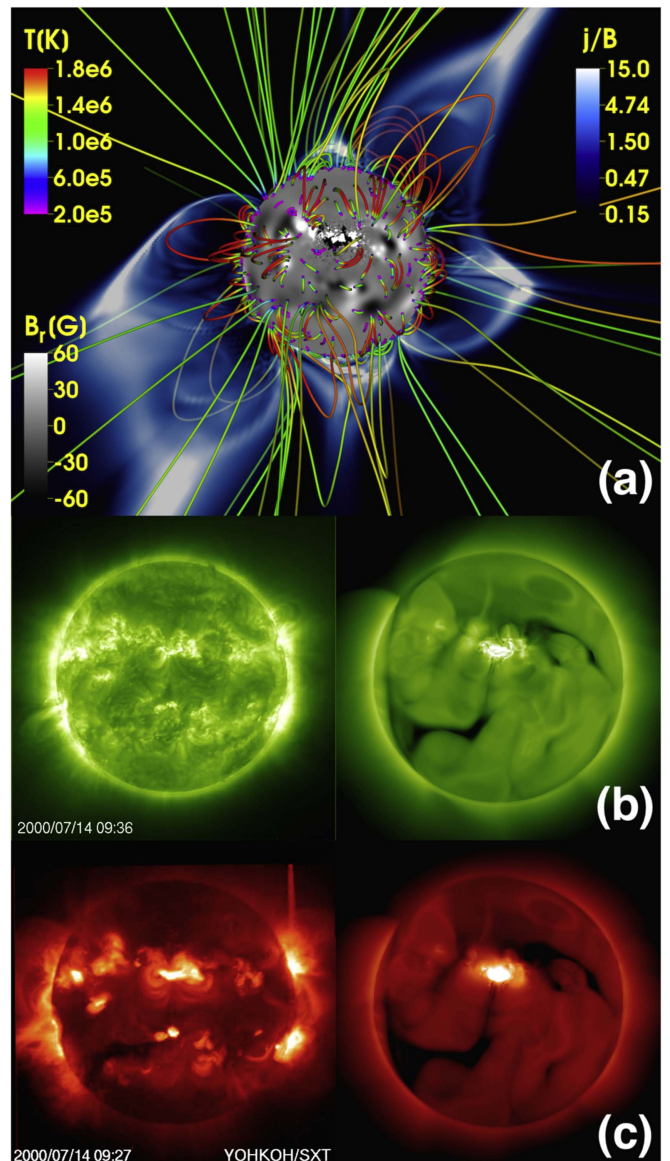

Figure 2. (a) Coronal configuration after the thermodynamic MHD relaxation ($t = 160$), seen from Earth at $\approx$09:30 UT on 2000 July 14. NOAA AR 9077 is located north of disk center. The quantity $|\boldsymbol{j}|/|\boldsymbol{B}|$ (in code units), where $\boldsymbol{j}$ is the current density and $\boldsymbol{B}$ the magnetic field, is shown in a transparent plane cutting through the Sun's center, outlining several streamers, that is, strong activity during the time of the Bastille Day event. Field lines are colored by plasma temperature. The radial magnetic field, B_r, at $R_\odot$ is saturated at 60 G, to visualize the heavily smoothed ARs outside NOAA AR 9077. (b) *SOHO*/EIT 195 Å observation of the corona at 09:36 UT on 2000 July 14, about half an hour before eruption (left), and synthetic emission obtained from the simulation at $t = 162$, after flux-rope insertion and MHD relaxation (right). Emission from smoothed and underresolved ARs outside NOAA 9077 is not visible in the synthetic image. (c) *Yohhoh*/SXT observation at a similar time, together with a synthetic *Hinode*/XRT image at $t = 162$.

field, which reintroduces the subtracted B_r so that B_{r0} is preserved. This configuration is then numerically relaxed toward a force-free state using a $\beta = 0$ MHD model (solution of the momentum equation and Faraday's law with zero plasma pressure, e.g., Mikić & Linker 1994). Since preservation of the magnetogram changes the potential field into which the flux rope is inserted, several trial-and-error attempts are required until a stable numerical equilibrium is found. The configuration shown in Figure 3(c) approached an approximately force-free equilibrium in about $0.2 \tau_A$ during the $\beta = 0$ MHD relaxation.
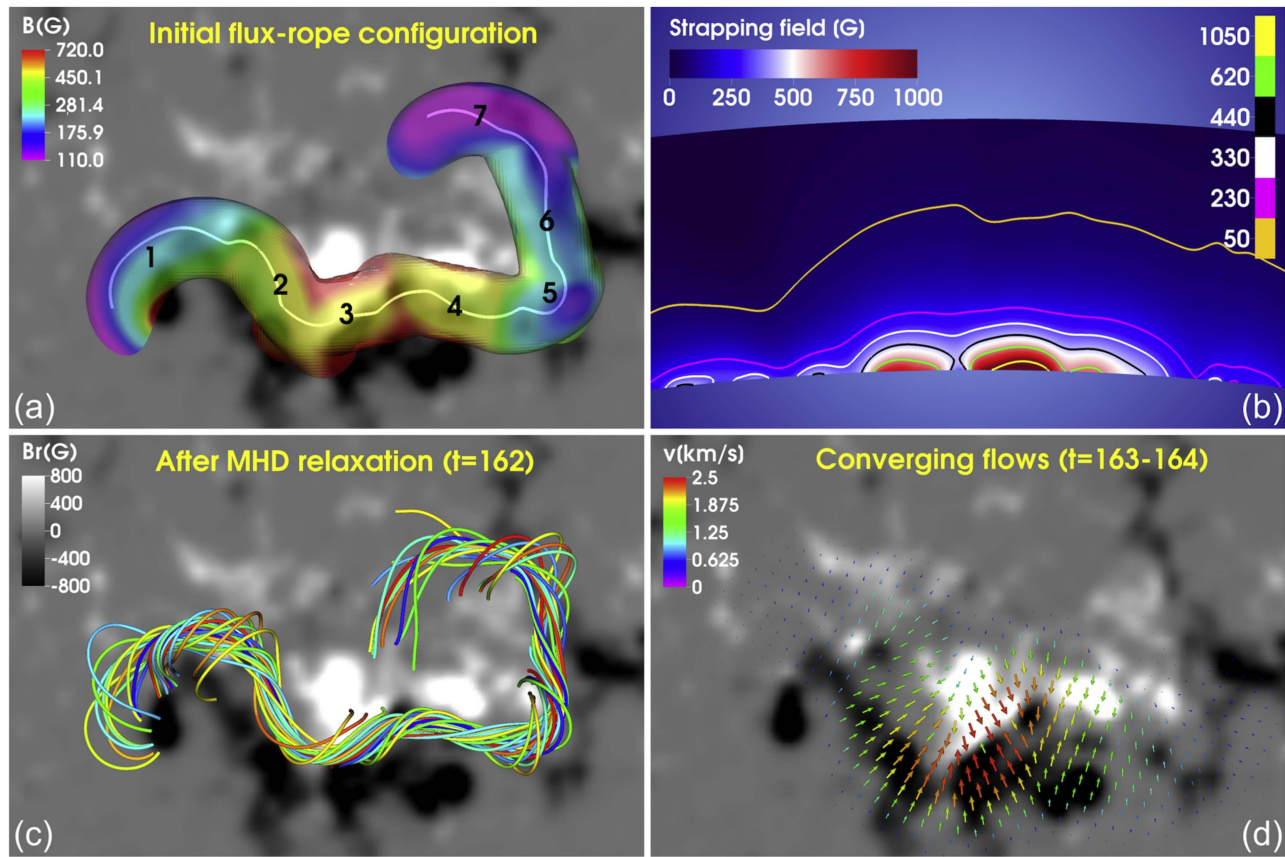
Figure 3. AR energization. (a) Flux rope prior to $\beta = 0$ relaxation, visualized by a transparent isosurface of $|j| = 0.04\,|j|_{\mathrm{max}}$, colored by $|B|$. The white line is the PIL at $r = 1.014\,R_{\odot}$, running roughly along the rope axis. Individual TDm ropes are numbered. Field lines are omitted for clarity; they would look similar to those in (c). (b) Strapping field for the PIL at $r = 1.01\,R_{\odot}$, in the height range $r = (1.0–1.1)R_{\odot}$, along a PIL segment that approximately covers TDm ropes 1–5 (from left to right). Selected strapping-field contours are shown. (c) Flux-rope field lines after rope insertion and subsequent MHD relaxation. (d) Converging-flow pattern used to trigger the eruption. See text for details.

To insert the relaxed flux rope into the corona, we work directly with the 3D vector potentials, A, that are advanced by MAS (Appendix A). To get the energized portion of the field only, we calculate $A_E = A_{\mathrm{ZB}} - A_{\mathrm{pot}}$, where A_{ZB} is the full vector potential of the $\beta = 0$ MHD solution, and A_{pot} is the vector potential of the corresponding potential field. We then add A_E to the full vector potential of the relaxed thermodynamic MHD model of the global corona, A_{cor}. These steps illustrate a useful way to insert energized fields from auxiliary computations or models (in our case the $\beta = 0$ flux-rope relaxation) while preserving the surface radial magnetic-field distribution of the global simulation.

3.2.2. Construction of Pre-eruptive Flux-rope Equilibrium

To construct our flux-rope configuration, we use the modified Titov–Démoulin (TDm) model (Titov et al. 2014), which is an extension of the original Titov–Démoulin (TD) model (Titov & Démoulin 1999). The latter is an analytical description of a force-free coronal flux-rope equilibrium that has found wide application as an initial condition for CME simulations (e.g., Roussev et al. 2003; Török & Kliem 2005; Schrijver et al. 2008a; Kliem et al. 2010; van Driel-Gesztelyi et al. 2014). TD flux ropes have been used also in some of the out-of-equilibrium simulations mentioned in the Introduction (e.g., Lugaz et al. 2011). In those cases, the external "strapping field" of the TD configuration, which runs perpendicular to the flux-rope axis and ensures magnetic equilibrium (Shafranov 1966), was removed, and the

flux rope was inserted into the modeled background field of the eruption's source region, roughly aligned with the region's PIL. This facilitates an immediate eruption of the rope, but neglects that real eruptions always start from a stable magnetic configuration, in which an expansion of the pre-eruptive flux is counteracted by the background magnetic field.

To provide this capability for CME simulations, the TDm model was designed to facilitate the construction of force-free flux-rope equilibria in an arbitrary background field, as long as that field is locally (i.e., on the length scale of the flux rope) bipolar. As in the TD model, the TDm flux rope is a partly submerged torus with constant field strength along its axis. The rope is placed in a given background field above the PIL such that its axis approximately follows an isocontour of the strapping field. The equilibrium current and axial flux of the rope are then determined using the strength of the strapping field along that contour (Titov et al. 2014). To obtain a stable equilibrium, the thickness (minor radius) and height of the rope above the surface must be chosen such that it is stable with respect to the ideal MHD kink and torus instabilities (e.g., Török et al. 2004; Kliem & Török 2006). With this technique, flux ropes can be introduced close to, but beneath, the threshold for eruption.

Before constructing a pre-eruptive configuration, we have to select the eruptive segment of the PIL along which to place a flux rope. For this we use *SOHO*/EIT and *Transition Region And Coronal Explorer* (*TRACE*; Handy et al. 1999) observations

of the flare arcades and filament eruptions shown in Figures 7 and 9. The two eruptions described in Sections 2 and 4.5 occurred successively at adjacent segments of the same PIL (see Figures 9(a), (b)). While our main goal is to model the first event, we decided to construct a flux rope that continuously covers both PIL segments, rendering the configuration more realistic and allowing us also to study the conditions that led to the second eruption.

Two challenges for constructing a single flux rope along the eruptive segment of the PIL with a single instance of the TDm model are evident from Figure 3. First, the segment is very elongated and highly curved (Figure 3(a)). Second, the strength of the strapping field strongly varies along it (Figure 3(b)). In contrast, the TDm flux rope possesses toroidal geometry (i.e., its axis is straight in projection to the surface), and the field strength is constant along the axial direction of the rope. While the model allows one to construct via numerical relaxation flux ropes that deviate from a strictly toroidal shape (see Figures 3 and 4 in Titov et al. 2014), it is not flexible enough to be used for source-region PILs as complex as the one in NOAA AR 9077.[2]

We therefore use seven individual, overlapping TDm flux ropes, placed as a chain along the eruptive segment of the PIL (Figure 3(a)). The ropes labeled 1–5 cover the area of the main event, while ropes 6 and 7 cover the area of the second eruption. Note that the respective field strengths of the ropes differ considerably, due to the large variation of the background field along the PIL. The choice of the geometrical parameters and of the field strength of the individual ropes is guided by the strapping-field contours shown in Figure 3(b). To obtain the strapping field, we choose the PIL at $r = 1.01\,R_\odot$, which roughly corresponds to the height we intend for the axis of the final flux rope. We then calculate the field component perpendicular to this PIL in the curved vertical plane defined by the PIL. The height of the pre-eruptive structure is not well constrained by the observations, so the choice of the strapping-field contours along which to approximately place the respective TDm ropes is somewhat arbitrary. Since we aim to maximize the free energy added to the system, we place the ropes relatively low in the corona, where the strapping fields are strong. However, since the ropes need to have a reasonable thickness (10 Mm or so), we cannot position them too close to the lower boundary. We experimented with different apex heights of the respective rope axes, and we found that a height range of $r \approx (1.01\text{–}1.015)R_\odot$ provides the best compromise.

Once the positions of the TDm ropes are determined, the axial-field direction of the whole structure has to be selected. We choose the direction (top right to bottom left in Figure 3) such that the flux rope is left-handed (negative helicity), which is suggested by photospheric vector data (Zhang 2002), observed soft X-ray loops, and linear force-free field extrapolations (Yurchyshyn et al. 2001), and by observations of the MC associated with the eruption (e.g., Lepping et al. 2001; Yurchyshyn et al. 2001; Lynch et al. 2005). Since adjacent TDm ropes overlap and their fields are superimposed, some axial flux connecting the two end points of the flux rope is present right away, before any numerical relaxation, while a considerable fraction of the axial flux

has to connect to the surface, due to the strong variations of the field strength along the flux rope.

3.2.3. Flux-rope Insertion and Relaxation

After inserting the flux rope into the global thermodynamic solution, we relax the combined system for about 50 minutes ($t = 160\text{–}162$). Figure 3(c) shows flux-rope field lines at $t = 162$. After the insertion, the resulting configuration is close to being force-balanced but is not in thermal equilibrium. Flows and plasma condensations appear along the flux-rope field lines, possibly arising from thermal nonequilibrium (e.g., Mikić et al. 2013a). During the relaxation, the numerical dissipation (enhanced by the thermal flows) leads to some loss of magnetic energy (see Figure 5). This slow but continuous loss of magnetic energy was the reason why we did not relax the system for a longer time period, which would have allowed the unphysical large-scale wave triggered by the rope insertion to fully leave the numerical domain. At the onset time of the eruption in our simulation ($t \approx 164$; see Section 4), this wave has traveled away from the source region to a distance of several $R_\odot$, which is sufficient for avoiding its interference with the actual eruption.

Figure 4 shows the simulated AR before and after the flux-rope insertion and subsequent MHD relaxation, viewed from the west along the main (east–west) section of the PIL. The top panels show synthetic emission images obtained from the simulation in the 171 Å passband of the Atmospheric Imaging Assembly (AIA; Lemen et al. 2012) on board the *Solar Dynamics Observatory* (*SDO*; Pesnell et al. 2012). Several loop-like features are visible (for the formation mechanisms of such loops, see, e.g., Mok et al. 2016). The remaining panels show the plasma temperature, number density, and electric currents in a vertical plane at the center of the AR, using the same view as for the emission images.

Prior to the insertion of the flux rope (left), the core of the AR is practically current-free and contains hot and moderately dense plasma. Stronger currents are present only around the tip of the streamer that overlies the AR. Surrounding the AR core, collimated regions of relatively cool and dense plasma are visible, resembling the loop-like features in the emission images. The area of very low density north of the AR (dark blue in Figure 4(c)) outlines the base of a coronal hole. After the rope insertion and subsequent relaxation (right), the flux-rope current is concentrated in a relatively small area above the surface and the streamer base has expanded, due to the increased amount of closed flux in the AR. The region of hot plasma has expanded as well, and its temperature has increased as a result of additional heating from the increased magnetic field strength (Lionello et al. 2009). It can be seen that cold and dense material accumulates just above the PIL, presumably due to plasma evaporation and subsequent condensation (e.g., Xia et al. 2014).[3] This "prominence" material appears bright in the synthetic emission image, since our optically thin assumption and procedure of creating such images do not take into account absorption or radiative transfer considerations for material at high densities and low temperatures (Mok et al. 2005). The plasma beta (the ratio of thermal to magnetic pressure) is small ($\approx 10^{-3} - 10^{-2}$) in the AR core, but increases to ≈ 1 toward the streamer tip. The Alfvén speeds in the AR core are in excess of

---

[2] We have very recently developed a new model that allows one to construct analytical flux-rope configurations with an arbitrary axis shape (Titov et al. 2018). This model would have strongly facilitated the construction of our complex pre-eruptive configuration, but it was not yet available when we performed the simulation described here.

[3] A detailed investigation of the mechanism(s) by which this prominence-like material forms is complex and beyond the scope of this article. It will be the subject of a future publication.
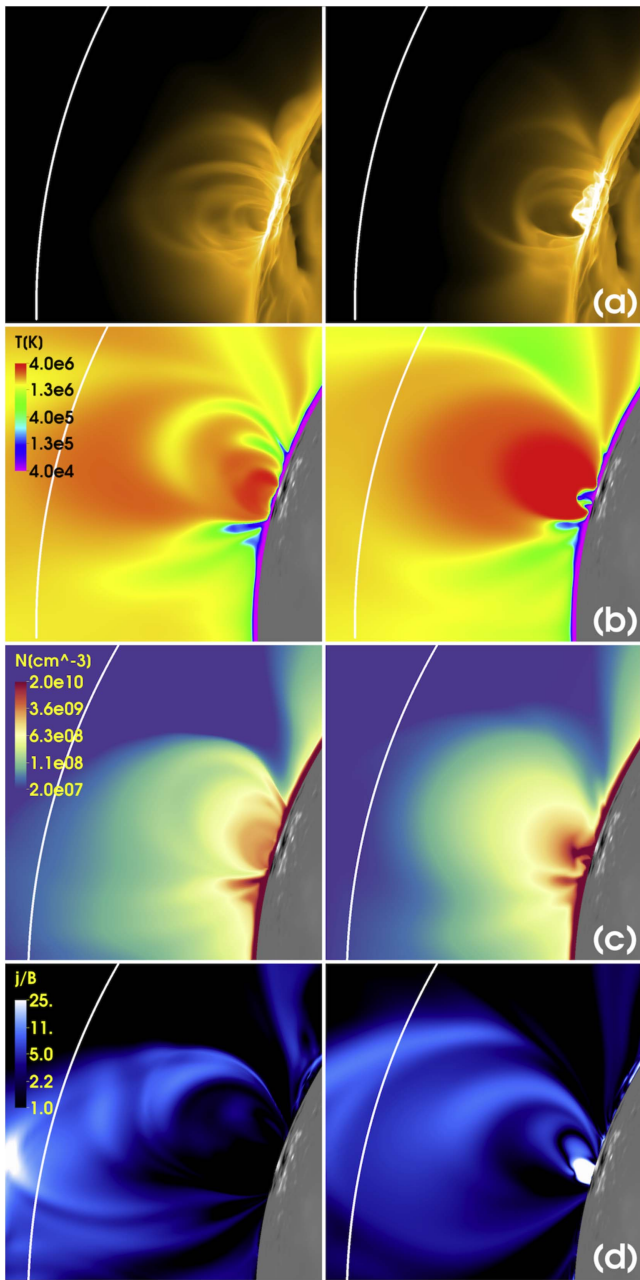
Figure 4. Simulated NOAA AR 9077 before (left; $t = 160$) and after (right; $t = 162$) flux-rope insertion and MHD relaxation, viewed from the west along the main (east–west) section of the PIL. The quantities in (b)–(d) are shown in a vertical plane roughly perpendicular to the PIL, located approximately in the center of the flux rope shown in Figure 3 (between TDm ropes 3 and 4). (a) Synthetic *SDO*/AIA 171 Å emission images. (b) Plasma temperature. (c) Number density. (d) $|\boldsymbol{j}|/|\boldsymbol{B}|$ (in code units). The white arc indicates the height $r = 1.5\,R_\odot$ (from Sun center) in all panels.

$10^4\,\mathrm{km\,s^{-1}}$. Outflows exceeding $100\,\mathrm{km\,s^{-1}}$ are present in the coronal hole region north of the AR, while the flows are only a few $\mathrm{km\,s^{-1}}$ in the AR core.

3.3. Initiation of the Eruption

After the flux-rope insertion and subsequent relaxation, we trigger an eruption by imposing at $r = R_\odot$ localized, sub-Alfvénic plasma flows that converge toward the PIL (e.g., Linker et al. 2003; Mikić et al. 2013b). Such flows serve to slowly expand the field overlying the flux rope and lead to flux

cancellation at the PIL. Both effects result in a slow rise and successive detachment of the rope until it becomes unstable and erupts (e.g., Aulanier et al. 2010). Flux cancellation was observed at several sites prior to the Bastille Day event and has therefore been suggested as a trigger mechanism for the eruption (e.g., Zhang et al. 2001). We impose the flows during $t = 162$–164 (for about 50 minutes). At $t = 164$, when the configuration destabilizes (see Section 4), we ramp them down linearly to zero within $0.05\,\tau_{\mathrm{A}}$.

The imposed flow pattern is shown in Figure 3(d). It is developed ad hoc, that is, not derived from flows measured on the Sun. However, we constrain the flow pattern by the observed evolution of the Bastille Day event, which started with the eruption of a filament at the western end of the east–west PIL section and then proceeded toward the east, successively building the flare arcade shown in Figures 7 and 9. We thus design our flows with the goal that the flux-rope sections labeled 4 and 5 in Figure 3(a) lift off first, followed by sections 1–3. No flows are imposed below sections 6 and 7, where the second eruption took place.

In our first attempts, we found that sections 4 and 5 indeed erupted, while sections 1–3 did not. This happened because in the narrow strong-field area between sections 3 and 4, field lines slowly but continuously disconnected from the rope and became attached to the strong flux concentrations at the surface. Then, when the eruption set in, the rope essentially split into two parts, one erupting, the other staying. The slow disconnection of the flux rope started already in the relaxation phase, indicating that the flux-rope field strengths in this narrow area were not chosen large enough to balance the downward-directed forces resulting from the interaction of the flux-rope current and the strapping field.

Rather than further optimizing our flux-rope configuration, we decided to prevent this undesired behavior by using a "two-step" flow pattern. During $t = 162$–163, we imposed flows localized below sections 3 and 4, to counteract the flux-splitting in this area. Afterwards ($t = 163$–164), we imposed the full pattern shown in Figure 3(d), which now led to the eruption of sections 1–3 as well. We eventually fine-tuned the flows further to achieve a smooth lift-off of the rope, progressing successively from section 5 toward section 1.

3.4. Interplanetary Simulation

To model the interplanetary propagation of the Bastille Day ICME to Earth, we couple the coronal simulation to the recently updated heliospheric version of MAS (Lionello et al. 2013; Merkin et al. 2016), which solves a simpler set of the MHD equations that neglects radiative losses, thermal conduction, and coronal heating in the energy equation, in either a corotating or inertial frame (Lionello et al. 2013). In the corotating frame, the Coriolis and centrifugal forces are included in the momentum equation. The heliospheric domain is advectively dominated (flows are supermagnetosonic) and is therefore less expensive computationally (as compared to the corona). A $1484 \times 272 \times 368$ nonuniform spherical mesh extending from $r = 19$ to $230\,R_\odot$ is used. To ensure a smooth transition of the CME from the coronal domain into the interplanetary one, we run the coronal simulation until $t = 188$ (≈ 9.6 hr after the onset of the eruption), at which time the CME has completely left the coronal domain. We then extract for the whole simulation period ($t = 160$–188) the variables $\boldsymbol{B}(t)$, $\boldsymbol{v}(t)$,

$\rho(t)$, and $T(t)$ at $r = 19\,R_{\odot}$, which are used to drive the interplanetary simulation.

We start by calculating a potential field in the heliospheric domain based on $B_r(t = 160)$. Then, using the variables B_r, v_r, ρ, and T at $t = 160$ as fixed boundary conditions in the corotating frame, we relax the interplanetary system for 800 τ_A, until a steady state is reached and the Parker spiral has formed, and reset the time to $t = 160$. This frame is advantageous as it allows us to concentrate the grid points in the heliospheric domain near the Sun–Earth line during the relaxation. To model the propagation of the ICME, we transform to the inertial frame and impose the variables $B_r(t)$, $v_r(t)$, $\rho(t)$, and $T(t)$ as time-dependent boundary conditions (now rotating with the solar rotation rate) at the inner boundary for the whole extracted period, $t = 160$–188. The remaining components of $\boldsymbol{B}(t)$ and $\boldsymbol{v}(t)$ are used for the calculation of the electric fields at the inner boundary, which determines the evolution of the tangential magnetic field. Finally, for $t > 188$, only the values of B_r, v_r, ρ, and T extracted at $t = 188$ are prescribed as fixed boundary conditions until the end of the simulation, while the remaining components of $\boldsymbol{B}$ and $\boldsymbol{v}$ are not included in the computation of the electric fields at the inner boundary. For more details on the coupling of the two codes, we refer the reader to Lionello et al. (2013).

4. Results: Coronal Evolution

Following the slow rise phase imposed by the converging flows, the configuration destabilizes shortly after $t \approx 164$, producing a fast CME and a flare. In this section, we first discuss the energy evolution of the eruption (Section 4.1), followed by a description of the overall evolution during the rapid acceleration phase in the low corona (Section 4.2). We then investigate the propagation of the CME in the outer corona (Section 4.3) and the EUV wave and dimmings associated with the CME (Section 4.4), and we compare both with available observations. Finally, we analyze a subsequent eruption that originates in the western section of NOAA AR 9077 (Section 4.5).

4.1. Energetics

Figure 5 shows the evolution of the magnetic and kinetic energies in the coronal domain before and after eruption. The insertion of the flux rope at $t = 160$ adds 2.6×10^{33} erg of free magnetic energy to the system, a considerable fraction of which is lost due to diffusion and thermal flows during the subsequent relaxation and converging-flow phases between $t = 160$ and $t = 164$. The eruption commences shortly after $t = 164$, releasing 1.33×10^{33} erg in about 4 minutes ($0.16\tau_A$); about 28% (3.74×10^{32} erg) is converted into kinetic energy. This is an important result, as it demonstrates that thermodynamic MHD simulations starting from a pre-eruptive configuration in magnetic equilibrium can reproduce the strong and fast energy release observed in extreme events (this was not clear previously; see the discussion in Mikić et al. 2013b). After about 5 hr, when the overlying streamer is beginning to settle back to an equilibrium, the total magnetic energy of the system has been reduced by 2.10×10^{33} erg.

It is instructive to compare the energies stored and released in the simulated AR to the AR potential-field and open-field energies W_{pot} and W_{open}, respectively. (For a given photospheric flux distribution, the open field is the magnetic field with all field
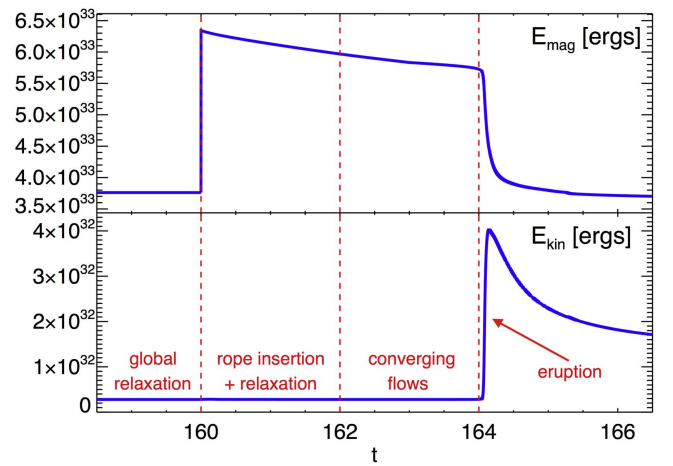

Figure 5. Magnetic and kinetic energies in the simulation around the Bastille Day eruption. Times are in τ_a ($\approx$24 minutes).

lines starting at the photosphere and extending to infinity.) Previously, it has been argued (Aly 1991; Sturrock 1991) that the energy of a force-free field cannot exceed W_{open}. If this "theorem" (not formally proven) is correct, it places an upper limit on the amount of free energy that can be stored, $W_{open} - W_{pot}$. We refer to this energy difference as the maximum free energy or MFE. Using the area shown in Figure 1(b) to compute $W_{pot} = 1.71 \times 10^{33}$ erg and $W_{open} = 5.76 \times 10^{33}$ erg for NOAA AR 9077, we obtain MFE $= 4.05 \times 10^{33}$ erg. The energy added to the simulated AR when the flux rope is inserted (2.6×10^{33} erg) corresponds to 64% of the MFE. Some of this energy is lost during the relaxation and converging-flow phases. The associated flux cancellation also reduces W_{open} and W_{pot}, reducing the MFE to 3.63×10^{33} erg at the onset of the eruption. Therefore, the total energy release during the simulated event (2.10×10^{33} erg) is about 58% of the MFE, 63% of which (37% of the MFE) is released impulsively, within the first 4 minutes after eruption onset. Our results thus suggest that the MFE is a useful upper bound for the maximum energy release of very large events. Another field, the partially open field (Wolfson & Low 1992; Hu 2004; Aly & Amari 2007), has been shown to provide a much tighter bound (Amari et al. 2007, 2014), but its computation is not trivial. The calculation of the partially open field for the Bastille Day event will be the subject of a future investigation.

4.2. Eruption

Figure 6(a) depicts the flux-rope core during the rapid acceleration phase, after the eruptive part of the flux rope has disconnected from the surface. The rope does not ascend fully radially, but a few degrees toward the south, due to a slight north–south asymmetry of the background magnetic field in the source region. At the time shown, a part of its western leg has reconnected with the background field, leading to a displacement of field lines. The reconnection occurs across a current layer associated with a pseudostreamer located next to the rope (see Section 4.5 and Figure 9). The flux rope quickly reaches a speed of $\gtrsim 2500\,\mathrm{km\,s^{-1}}$, which leads to a strong compression of the plasma and the magnetic field in front of it and to the formation of a shock (since the background Alfvén speed is exceeded). The shock forms low in the corona, below a height of $1.5\,R_{\odot}$. It is visible in Figure 6(a) as a layer of strong current surrounding the flux rope. Such low-coronal shocks (or plasma
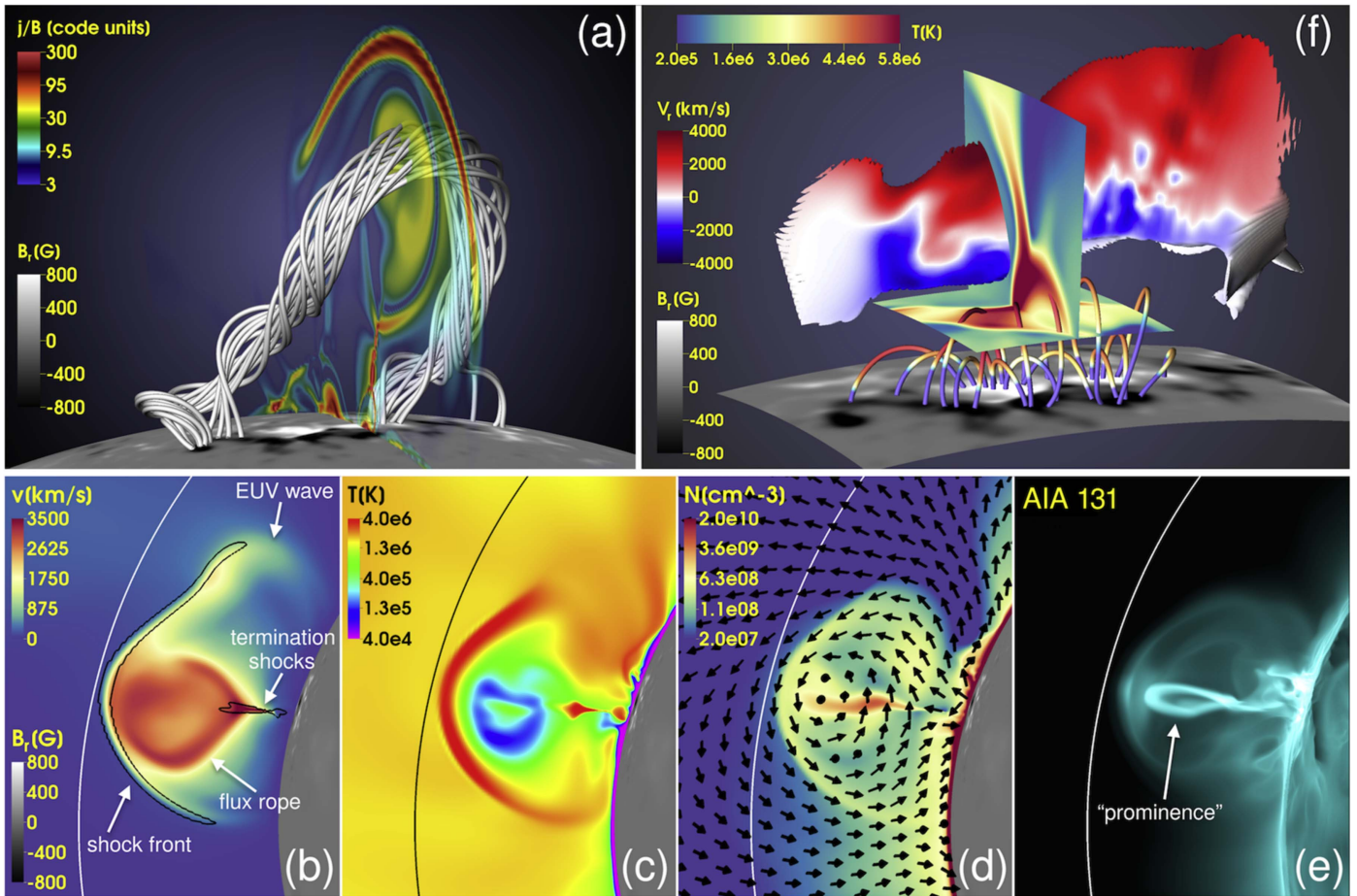
Figure 6. Various quantities during the eruption. (a) Field lines of the flux-rope core at $t = 164.10$, shortly after eruption onset. $|j|/|B|$ is shown in a transparent plane perpendicular to the rope axis, depicting flux-rope currents, the current layer below the rope, and a compression region (shock) in front of the rope. (b)–(d) Plasma velocity, temperature, and number density in the same plane as in (a), at $t = 164.12$, about 30 s later. Black contours in (b) show $\nabla \cdot v = -0.025$ s^{-1}; arrows in (d) show the magnetic field vector. (e) Synthetic AIA 131 Å image. Arcs in (b)–(e) mark $r = 1.5\,R_\odot$. (f) Visualization of reconnection below the flux rope, at $t = 164.24$, about 4 minutes after eruption onset. The main section of the elongated current layer is shown as an isovolume of $|j|/|B|$, colored by v_r (depicting reconnection outflows). Plasma heating is visualized in two plane segments showing temperature. Reconnected field lines, colored by the same temperature scale, are shown below the current layer. The center of the current layer is removed to reveal the high-temperature cusp in the vertical plane segment.

and magnetic field compressions) are a preferable site for the efficient acceleration of particles to high energies (e.g., Schwadron et al. 2015). A vertical current layer has started to form below the erupting rope, across which flare reconnection takes place.

Figures 6(b)–(e) show the eruption about 30 s later, when the shock has almost reached $r = 1.5\,R_\odot$ and the EUV wave associated with the eruption has started to disconnect from the flux rope in the northern direction, where the Alfvén speed is larger (see also Section 4.4). We overlaid the velocities in Figure 6(b) with a contour of $-\nabla \cdot v$ to visualize the locations of fast-mode shocks (Forbes 1990). Apart from the shock wave in front of the flux rope, two termination shocks form below it. They result from the very fast flare-reconnection outflows, which locally reach 10^4 km s^{-1}. Figures 6(c), (d) show that dense and cold plasma is carried upward by the flux rope, the center of which can be inferred from the magnetic-field vectors shown in Figure 6(d). Note that the field direction is approximately parallel in front of the rope; that is, the current layer that precedes it does not form due to the perturbation of a null point or null line, as is the case in quadrupolar configurations (e.g., Antiochos et al. 1999). The plasma surrounding the flux rope is heated to temperatures of up to

≈ 6.3 MK at the time shown, presumably by compressional heating (joule heating was not included in the simulation; see Appendix A). The temperature further increases as the eruption evolves, reaching ≈ 10.9 MK (below a height of $r \approx 2\,R_\odot$), after which it starts to decrease. Strong heating occurs also above and below the flare-reconnection region, where the plasma reaches peak temperatures of ≈ 9.5 MK.

Figure 6(e) shows a synthetic AIA 131 Å image in the same view for comparison. A bubble-like structure, with its edge corresponding to the density and temperature enhancements surrounding the rope, is clearly visible. Note that the bright, loop-like feature in the center is not a "hot flux-rope core," as frequently observed by AIA (e.g., Cheng et al. 2011). The temperatures in this area are much too cold to produce emission in the hot peak of the response function in this wavelength (≈ 10 MK). The feature rather outlines dense and mostly cold plasma that has accumulated in the corona during the pre-eruptive phase (see Figure 4) and is now carried away by the erupting flux rope (some of this "prominence" material probably stems from the chromospheric layer of our model, lifted upward by field lines that were initially penetrating that layer). This plasma appears bright in the emission image (see Section 3.2). In real observations, the loop-like feature would
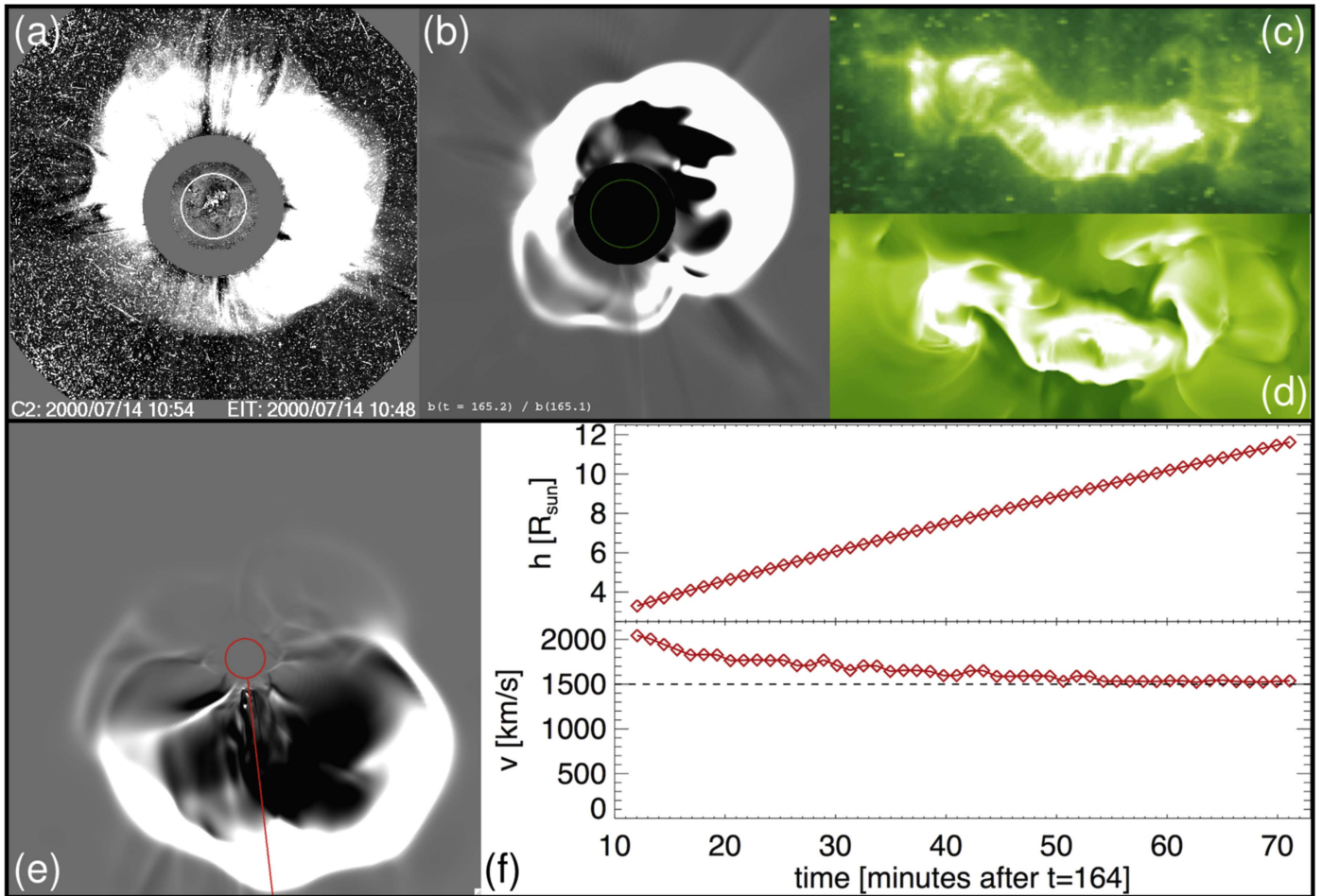
Figure 7. (a) *SOHO*/LASCO C2 difference image of the halo CME associated with the Bastille Day eruption. (b) Synthetic coronagraph image obtained from the simulation, showing running-ratio brightness at $t = 165.2$, as viewed from Earth. The field of view (FOV) is 1.5–6 $R_\odot$; the green circle marks the solar surface. (c) Flare arcade as seen by *SOHO*/EIT in 195 Å. (d) Corresponding synthetic emission image obtained from the simulation. (e) Same as (b), shown looking down on the ecliptic above the north pole of the Sun, at $t = 167$, corresponding to the last data point in (f). The red circle outlines the solar surface; the FOV is 1–12 $R_\odot$. (f) Height and velocity of the simulated CME leading edge in the range $\approx(3–12)R_\odot$. The data points were obtained along the red line shown in (e), using running-ratio brightness images.

appear mostly dark in the image, resembling an erupting filament.

Figure 6(f) shows the configuration a few minutes later. The flux rope has left the field of view at this time. Below the rope, a long and elongated current layer has formed, whose shape follows the eruptive part of the PIL. The coloring of the current layer depicts the flare-reconnection outflows, which are still several $1000\,\mathrm{km\,s^{-1}}$ at this time. Hot reconnected field lines have formed below the layer. They make up the flare arcade shown in Figures 7(c) and 9(a). A cusp-shaped hot plasma region is visible in the vertical plane segment, while the horizontal plane segment outlines the shape of the flare arcade. In a future study, we will address the details of plasma heating and energy transfer during the flare reconnection, which has so far been attempted only for very idealized configurations (e.g., Yokoyama & Shibata 2001; Birn et al. 2009; Reeves et al. 2010).

4.3. Evolution in the Outer Corona

In Figure 7 we compare the simulation with white-light and EUV observations at a later state, after the leading edge of the modeled CME has reached a height of several $R_\odot$. Figure 7(a) shows the halo CME observed with the Large Angle and Spectrometric Coronagraph (LASCO; Brueckner et al. 1995) on board *SOHO*. For comparison, we present in Figure 7(b) a synthetic running-ratio brightness image. A halo-like structure similar to the observed one can be seen; the fainter feature in the southeast is produced by the large-scale wave associated with the eruption (see Section 4.4). Note that the real halo is fainter at this location as well. Figure 7(c) shows emission from the flare in the *SOHO*/EIT 195 Å filter at 11:12 UT, $\approx$50 minutes after the flare peak seen in *GOES* (e.g., Andrews 2001). The flare loops were noted for their striking morphology and pattern of growth from west to east. Figure 7(d) shows synthetic EIT 195 Å emission from the simulation, which reproduces the overall morphology of the flare arcade quite well. The west-to-east growth of the arcade (not shown) is also reproduced qualitatively.

Figure 7(e) shows the CME in a view onto the ecliptic, at $t = 167$ ($\approx$1.2 hr after eruption), with the direction to Earth being toward the south in the image. We used a sequence of running-ratio brightness images in this view to produce the height–time profile shown in Figure 7(f), where the position of the leading edge was always measured along the red line. It can be seen that the CME slowly decelerates from its peak speed of $\gtrsim 2500\,\mathrm{km\,s^{-1}}$ (Section 4.2) as it travels in the solar wind, until
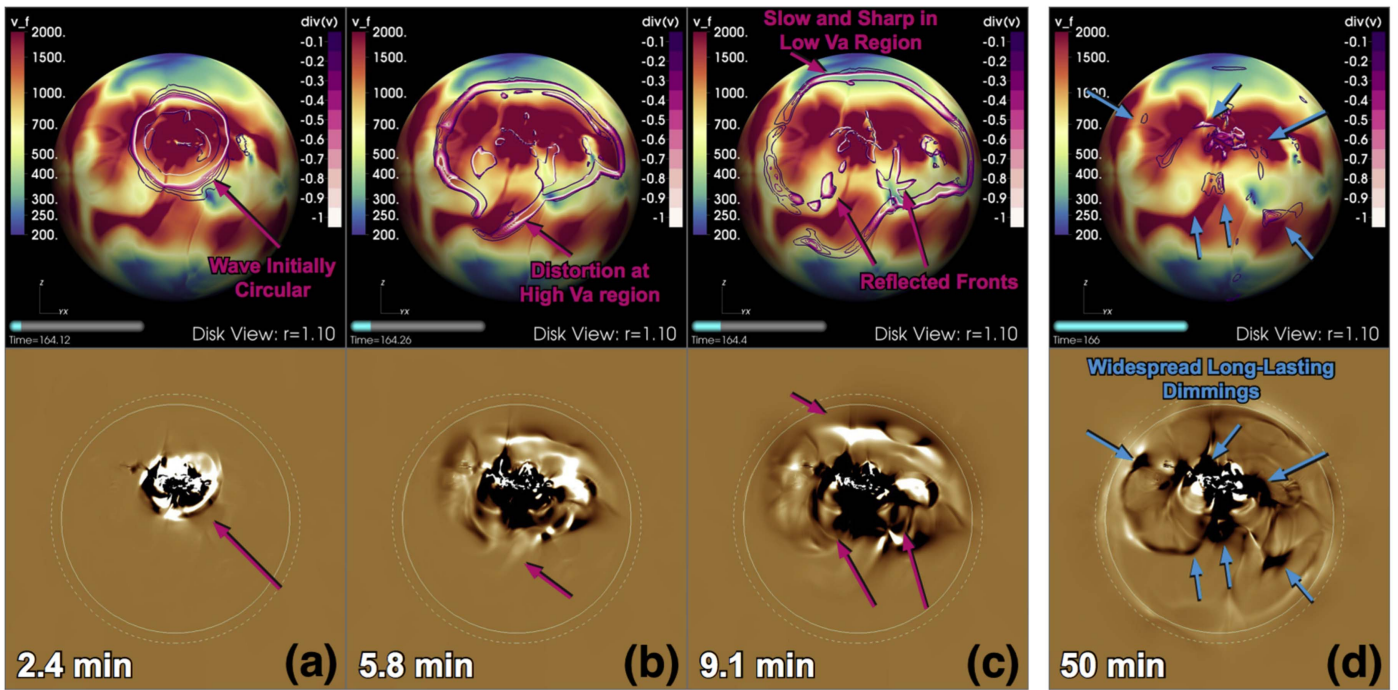
Figure 8. Visualization of the global EUV wave and coronal dimming features present in the simulation. The top panels show v_f [km s^{-1}] on a sphere taken at $r = 1.1 R_\odot$, with accompanying contours of negative $\nabla \cdot \boldsymbol{v}$ (in code units) to highlight the wave. The bottom panels show synthetic base-difference AIA 193 Å images. The solid and dashed lines in those images indicate distances of $r = 1.01$ and $1.10\ R_\odot$, respectively. (a)–(c) Simulation 2.4, 5.8, and 9.1 minutes after the eruption onset; arrows indicate interesting wave features; they are at the same positions in the top and bottom rows. (d) Persistent dimming features 50 minutes after eruption onset.

it reaches an almost constant propagation speed of about 1500 km s^{-1}, somewhat less than the observed peak propagation speed of ≈ 1700 km s^{-1} (Andrews 2001). Note, however, that the simulated CME does not move with the same speed in all directions; see also Figure 5 in Andrews (2001). In the low corona, this is due to the presence of background regions with different Alfvén speeds, and possibly also because the underlying flux rope erupts successively along the PIL. The resulting distortion of the CME shape amplifies as the ejecta travels in regions of nonuniform solar wind speed (see Section 5 and Figure 10).

4.4. Global Coronal Disturbances

The simulation allows us also to examine the response of the global corona due to the CME. Large-scale propagating coronal waves, or EUV waves (e.g., Warmuth 2015), are commonly associated with CMEs in the low corona, and we can clearly identify such a feature in the simulation. The top row of Figure 8 shows the perpendicular fast-mode magnetosonic wave speed, $v_f = \sqrt{v_a^2 + c_s^2}$, where v_a is the Alfvén speed and c_s is the sound speed, at a height of 1.1 $R_\odot$ along with negative contours of $\nabla \cdot \boldsymbol{v}$, which are useful for capturing the outer front of a compressible wave (e.g., Wang et al. 2009). Figures 8(a)–(c) follow the evolution about 2.4, 5.8, and 9.1 minutes after the eruption. The expansion of the CME introduces a strong, initially circular front, which rapidly distorts according to the local fast-mode speed. In the east and west directions, the front expands much more rapidly because of the persistently large v_f, while it slows and sharpens to the north where v_f drops rapidly to quiet-Sun values (200–300 km s^{-1}). In the south–southeast direction, a noticeable distortion is present where the wave expands into a high-v_f

region, which is adjacent to a low-v_f region to its west. At later times, secondary fronts or reflections at the high-to-low or low-to-high speed interfaces are also visible. Such behavior, distortions and reflections, are to be expected if the wave propagates at or slightly above the local magnetosonic speed. This result is also consistent with previous simulations (e.g., Schmidt & Ofman 2010; Downs et al. 2012).

The bottom panels of Figure 8 show the corresponding EUV evolution using synthetic AIA 193 Å base-difference images. Although the signal is difficult to compare one-to-one to the fast-mode speed at 1.1 $R_\odot$, because of significant projection effects and local variations of the ambient coronal temperature, there is a qualitative correspondence to the outer shape of the 193 Å front and the distortions in $\nabla \cdot \boldsymbol{v}$ shown in the top panels. Note that the outer EUV wave front appears dark in AIA 193 Å because the ambient 1.7–2.0 MK temperature of the model corona surrounding the erupting AR is slightly above the $\sim$1.5 MK peak temperature response of the 193 Å channel. This means that the compression and temperature enhancements due to the initial wave passage can lower the LOS emissivity (as discussed in the appendix of Downs et al. 2012). Such behavior is quite common for EUV waves in the AIA 171 Å channel (Nitta et al. 2013), but is sometimes also observed in the AIA 193 Å channel.

For the actual Bastille Day event, it was difficult to identify a clear coronal EUV wave, partially due to the 12-minute cadence limitation of EIT and the considerable amount of "snow" in the images caused by the strong release of energetic particles during the event. Andrews (2001) did not find any clear wave signatures but argued that the observed dimmings indicate the presence of a wave, while Chertok & Grechnev (2005) claimed that a weak wave with a propagation speed of ≈ 200 km s^{-1} was visible to the northwest, where no ARs were
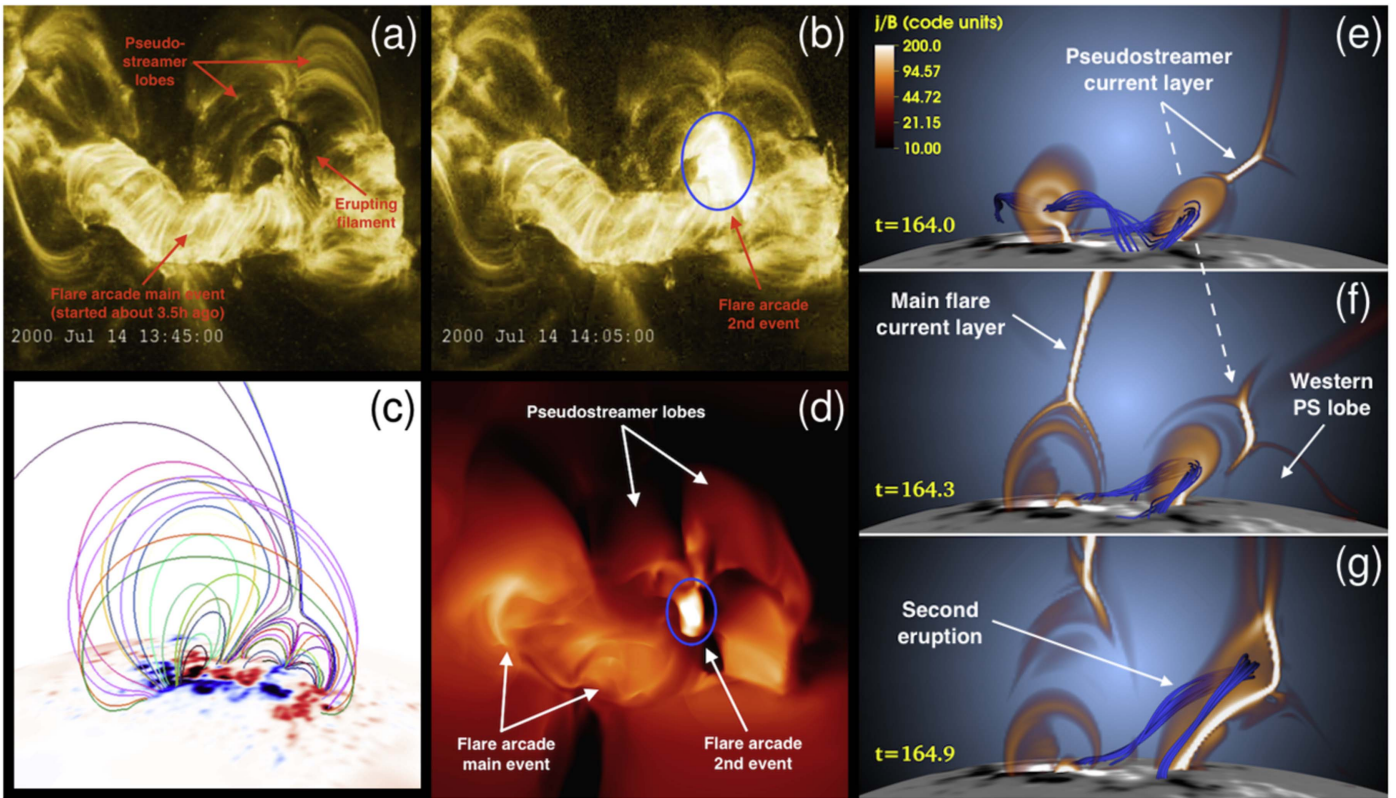
Figure 9. *TRACE* observations and simulation of the eruption that occurred ≈3.5 hr after the Bastille Day event. (a) Erupting filament. The Bastille Day flare arcade and the PS lobes are highlighted. (b) Flare arcade (encircled) 20 minutes later. (c) Potential-field extrapolation showing the PS structure. (d) Synthetic *Hinode*/XRT Ti_Poly image during the simulated eruption ($t = 165.3$). The flare emission is encircled. (e)–(g) Simulation at three consecutive times, showing flux-rope segments (blue field lines) and electric currents ($|j|/|B|$; orange-white) in a transparent vertical plane that intersects the flux rope approximately where, respectively, TDm ropes 3 and 4 and 6 and 7 overlap (see Figure 3(a)).

present. They mention that projection effects made it difficult to measure the kinematics accurately, but their estimation is roughly consistent with the magnetosonic speed at 1.1 $R_\odot$ in the quiet-Sun region to the north in our simulation. Using a height–time base-difference analysis for the northern part of the front in the synthetic EUV images, we estimate a somewhat higher speed of ≈300 km s^{-1}.

Lastly, a major discussion of Chertok & Grechnev (2005) was of the coronal dimmings visible in EIT 195 Å at large transverse distances from the erupting AR. These dimmings were visible for at least one hour after the eruption and might indicate long-lasting density depletion related to the CME or coronal reconfiguration. The bottom panel of Figure 8(d) shows a synthetic AIA 193 Å base-difference image about 50 minutes after the eruption (AIA 193 Å is very similar to EIT 195 Å). This is long after the bulk of the CME has left the low corona, and yet we see long-lasting dimming features in the simulation as well. The extended distribution of these dimmings over the solar disk bears a qualitative resemblance to those shown in Figure 1 of Chertok & Grechnev (2005). A detailed investigation of the relationship of these dimmings to the large-scale magnetic connectivity of the CME and the background corona is beyond the scope of this article; it will be the subject of a future study.

4.5. Second (Sympathetic) Eruption

The Bastille Day event was followed ≈3.5 hr later by a second eruption that took place at the western edge of NOAA AR 9077, along the north–south section of the PIL (roughly at

the location of TDm rope 6 in Figure 3(a)). It produced a filament eruption and an M3.7 flare with onset and peak times at 13:44 and 13:52 UT, respectively (Andrews 2001). Figures 9(a) and (b) show, respectively, the rising filament and the flare arcade observed by *TRACE*. The flare arcade of the Bastille Day event is still visible at this time. It is not clear whether a CME was associated with the second eruption, since the energetic particles produced by the Bastille Day event saturated the detectors of the *SOHO*/LASCO coronagraph until the next day. The filament may have initially been connected to the one that erupted during the main event; this is difficult to deduce from the observations. Prior to its eruption, it was located in the eastern lobe of a pseudostreamer (PS). The two lobes of the PS are clearly visible as adjacent loop arcades in the *TRACE* images, and the underlying magnetic structure is present in our simulation (Figure 9(c)). We note that the PS stalk, while reaching high into the corona, eventually closes back to the solar surface in our model. The structure is therefore not a classical PS, whose stalk would extend into interplanetary space. This difference is, however, irrelevant for the eruption scenario discussed in this section.

It has been shown that PSs provide a favorable environment for "sympathetic" eruptions (e.g., Török et al. 2011; Panasenco & Velli 2012; Titov et al. 2012, 2017; Lynch & Edmondson 2013). This is because above the lobes of a PS a magnetic null line is present that, when perturbed for instance by an external eruption, transforms into a current sheet across which magnetic reconnection takes place. The reconnection transfers magnetic flux from one lobe to the other, which may destabilize

a filament (or flux rope) that resides in the lobe whose flux is decreasing. Subsequently, flare reconnection induced by the eruption of this rope removes flux from the other lobe, which may trigger another eruption if a flux rope is present in that lobe (for a more detailed description of these processes, see Török et al. 2011). Note that this scenario for sympathetic eruptions is not restricted to PSs. It can occur in any magnetic configuration with adjacent closed-flux systems rooted in one common polarity and overlaid by a null line, for instance, in quadrupolar configurations (e.g., DeVore & Antiochos 2005; Peng & Hu 2007; Shen et al. 2012b; Yang et al. 2012; Joshi et al. 2016).

The relatively small time interval between the two eruptions, and the fact that the second eruption originated in a PS lobe, suggests that the eruptions were sympathetic, that is, that the Bastille Day event triggered the second eruption. This is difficult to establish from the observations, but we can turn to the simulation to search for clues.

Figures 9(e)–(g) show snapshots from the simulation at three consecutive times. Figure 9(e) shows the AR configuration in a view from the southwest, just before the first eruption sets in. The blue field lines outline the core of the flux rope, the very eastern part of which is not visible in the computational subdomain chosen for this illustration (see Figure 3(c)). The section of the rope that is located along the east–west section of the PIL is slowly rising, while the western section, which is located below the eastern PS lobe and is not affected by the converging flows (see Figure 3(d)), remains at its original position. Note that at this time the orientation of the current layer above the PS lobes is oriented such that reconnection across it would transfer flux from the western PS lobe to the eastern one, suppressing a second eruption rather than triggering it.

However, as the first eruption proceeds, it initially pushes both PS lobes to the west and downward. Then, after the flux rope has reached a certain height, the PS lobes start to expand and relax back to their old position. During this expansion, the orientation of the current layer reverses (Figure 9(f)). It is this change of orientation that allows the second eruption to occur, since the current layer is now oriented such that the reconnection driven by the expansion of the lobes removes stabilizing flux from the eastern PS lobe. Indeed, as illustrated in Figure 9(g), this finally leads to the eruption of the remaining flux-rope section. The trigger mechanism of the eruption is the same as described in Török et al. (2011).

It is important to note that the second eruption occurs self-consistently in the simulation, without boundary driving or any other external perturbation. The converging flows used to trigger the first eruption are fully switched off at $t = 164.05$, that is, before the second eruption starts around $t = 164.9$ (about 20 minutes after the first event). Thus, even though the second eruption occurs much earlier in the simulation than in reality, the simulation supports the conjecture that the two eruptions were sympathetic. The discrepancy between the modeled and observed onset time is not surprising. The onset time of the second eruption depends in a very sensitive manner on the detailed structure and evolution of the configuration. The degree of realism that would be required to reproduce the exact onset time is not available in numerical simulations, which are always only a simplification of reality. We note, for complete-ness, that Wang et al. (2006) suggested that the Bastille Day event was triggered by the almost simultaneous eruption of a large transequatorial filament. Since that eruption is not modeled in our simulation, we cannot test this suggestion.

5. Results: Interplanetary Propagation

The Bastille Day event was associated with an ICME (and MC) that triggered a large geomagnetic storm at Earth (Section 2). We modeled the ICME propagation in the inner heliosphere as outlined in Section 3.4. In this section we describe the resulting evolution, focusing on the ICME's arrival at Earth.

5.1. ICME Shape and Trajectory

Figure 10(a) shows the inner heliosphere with the Parker spiral prior to the Bastille Day event, visualized by electric currents (outlining the heliospheric current sheet) and plasma flows in the equatorial plane. The solar wind is highly structured; in other words, it contains regions of different plasma flow speeds, with compression regions generated where faster flow follows slower wind, and rarefaction regions where the reverse occurs. The overall wind speed appears to be somewhat large. In our model, it is predominantly determined by the choices made for the coronal heating and the Alfvén-wave pressure (see Appendix A). The former was guided by the observed coronal emission (Section 3.1), while the latter was based on our experience from previous solar wind simulations. Since a direct comparison with the solar wind conditions at Earth was not possible due to the strong activity preceding the Bastille Day ICME for almost a week, and since we do not expect that a somewhat slower overall wind would significantly affect the propagation of the ICME, we refrained from experimenting "blindly" with these parameters.

It has been suggested that inhomogeneous solar wind speeds lead to distortions of the ICME shape (e.g., Manchester et al. 2004; Owens 2006; Savani et al. 2010). This indeed happens in our simulation, as can be inferred from the electric currents shown in Figures 10(b), (c). The weaker currents at the backside of the central sphere (as seen from Earth) are associated with the large-scale wave triggered by the eruption rather than the actual ICME magnetic field. The most pronounced distortion is located to the west of Earth, corresponding to a part of the ICME that moves significantly faster than the background solar wind. Adjacent ICME sections do not seem to expand much faster than the wind; those show a clear association between shape distortion and locally enhanced wind speed. Strong deformations of the ICME occur elsewhere in the volume too. For instance, three pronounced "notches" can be seen in Figure 10(d). Those are at locations where the ICME intersects regions of slow wind surrounding the heliospheric current sheet, which are visible in the image as dark "lanes" of enhanced currents. These ICME distortions will become important later on, when we discuss the 1 au signatures derived from the simulation (Section 5.4). Note in Figure 10(c) the presence of an Earth-directed, fast stream behind the ICME front, which is not present prior to the appearance of the ICME. Such streams have been reported to occur frequently behind MCs (Fenrich & Luhmann 1998).

Figure 10 does not suggest any significant deflection of the ICME trajectory along the east–west direction (Wang et al. 2002). According to Wang et al. (2004), fast ICMEs should be deflected to the east, due to a pile-up of magnetic field at their front that is due to the presence of the Parker
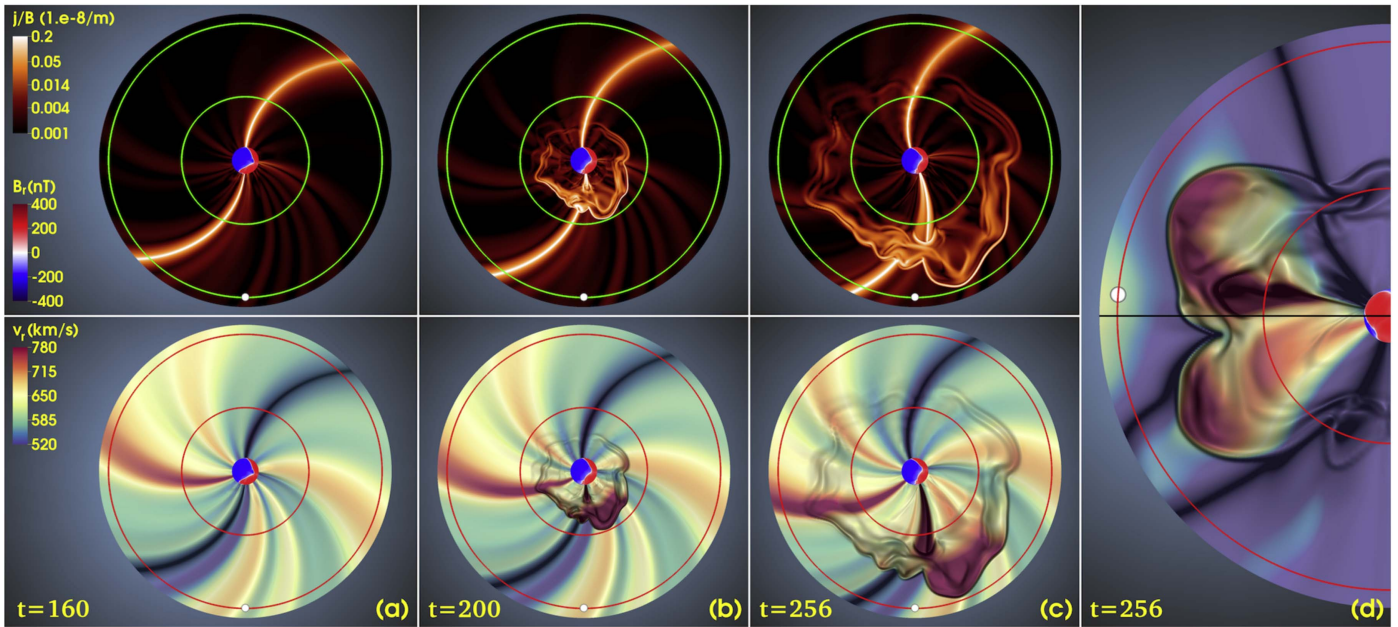
Figure 10. Interplanetary run. (a)–(c) Electric currents (top) and v_r with currents overlaid (bottom) in the equatorial plane ($\theta = \pi/2$). The view is onto the Sun's north pole. The central sphere shows B_r at $r = 21\,R_\odot$; circles mark $r = 100$ and $215\,R_\odot$. The white sphere shows Earth's position upon arrival of the MC at $r = 215\,R_\odot$. Earth is located $4.5°$ (the B_0 angle at this time) above the equatorial plane. (a) Background configuration 1.6 hr before the Bastille Day eruption. (b) 14.5 hr after the eruption; the ICME tip has reached $r = 100\,R_\odot$. (c) 37.0 hr after the eruption, ≈ 1.2 hr before the ICME arrives at $r = 215\,R_\odot$. (d) Same as (c) in the vertical plane ($\phi = 5.45$) that crosses Earth.

spiral. On the other hand, as those authors point out, fast events should be less susceptible to deflection than slow events. The lack of deflection in our case may indeed be due to the relatively fast ICME speed, but perhaps also due to a suppression of a significant pile-up of flux by continuous reconnection between the ICME and the interplanetary magnetic field.

5.2. ICME Magnetic Structure

Figure 11 summarizes the magnetic structure of the ICME flux rope, shortly before it reaches 1 au. Figure 11(a) shows field lines of the interplanetary magnetic field and the flux rope colored by the radial plasma flow. The overall shape of the rope is distorted (see Figure 10), and it can be seen that different sections move at different speeds. The two "bulges" at the front of the rope travel with a speed of $\approx 850\,\mathrm{km\,s^{-1}}$, significantly faster than the ambient solar wind.

To gain a better understanding of the magnetic structure, we use the squashing factor, Q (e.g., Titov et al. 2002; Titov 2007; Pariat & Démoulin 2012; Liu et al. 2016; Tassev & Savcheva 2017; see Appendix B), which allows one to identify distinct flux systems in complex magnetic fields (e.g., Titov et al. 2017). We calculate Q in a slice segment centered around the location of the MC, which we infer from our synthetic in situ data (see Section 5.3). This segment is shown in Figure 11(e); its location in the volume is shown in Figure 11(f). Dark lines of high Q outline the boundaries between flux systems with different properties. To aid our analysis, we superimpose in Figure 11(d) the Q map onto an "L map," which shows the total length, L, of the field lines.

Drawing field lines guided by the Q and L maps reveals two closed flux bundles of predominantly axial field (Figure 11(b)), which we hereafter refer to as the "core flux." The location of the core flux areas in the Q map is indicated in Figure 11(d). The remaining structure of the ICME flux rope is more

complex. In Figure 11(f) we show representative field lines that were integrated starting from various Q-map areas that surround the core flux (the starting points are indicated in Figure 11(e) by little spheres of the same color). Note that the two core flux bundles are separated from one another by two other flux bundles of different type. Those consist, respectively, of relatively long, closed field lines (red) that wrap around the core flux, and of field lines that apparently were part of the core flux but have reconnected with the interplanetary field and are now open (blue). The green, yellow, and light purple field lines are similar to the red one. They all represent closed flux bundles of rather distorted shape that wrap around the core flux in different ways (note that the red and light purple field lines cross the Q map twice). The dark purple field line represents open flux that has been distorted by the ICME (see also Figure 11(a)). Finally, the brown field line partially wraps around the core flux but is open at both ends; that is, it represents a fully disconnected flux that penetrates the ICME flux rope.

Our analysis shows that the basic magnetic structure of the initial coronal flux rope essentially survives during its propagation in the corona and interplanetary space. However, due to reconnection, likely ongoing at several sites as a result of interaction with the ambient solar wind, the structure becomes increasingly complex. Field lines get distorted into complicated shapes, the core axial flux is intruded by both open and closed twisted flux and eventually splits into two distinct domains, and the flux rope gets pervaded by disconnected flux. A detailed analysis of these processes would be beneficial for improving our understanding of how flux distributions change during the propagation of CMEs from the Sun to the Earth (e.g., Gopalswamy et al. 2017), for studying related aspects such as flux erosion of CMEs and ICMEs (e.g., Manchester et al. 2017), and for benchmarking and potentially improving
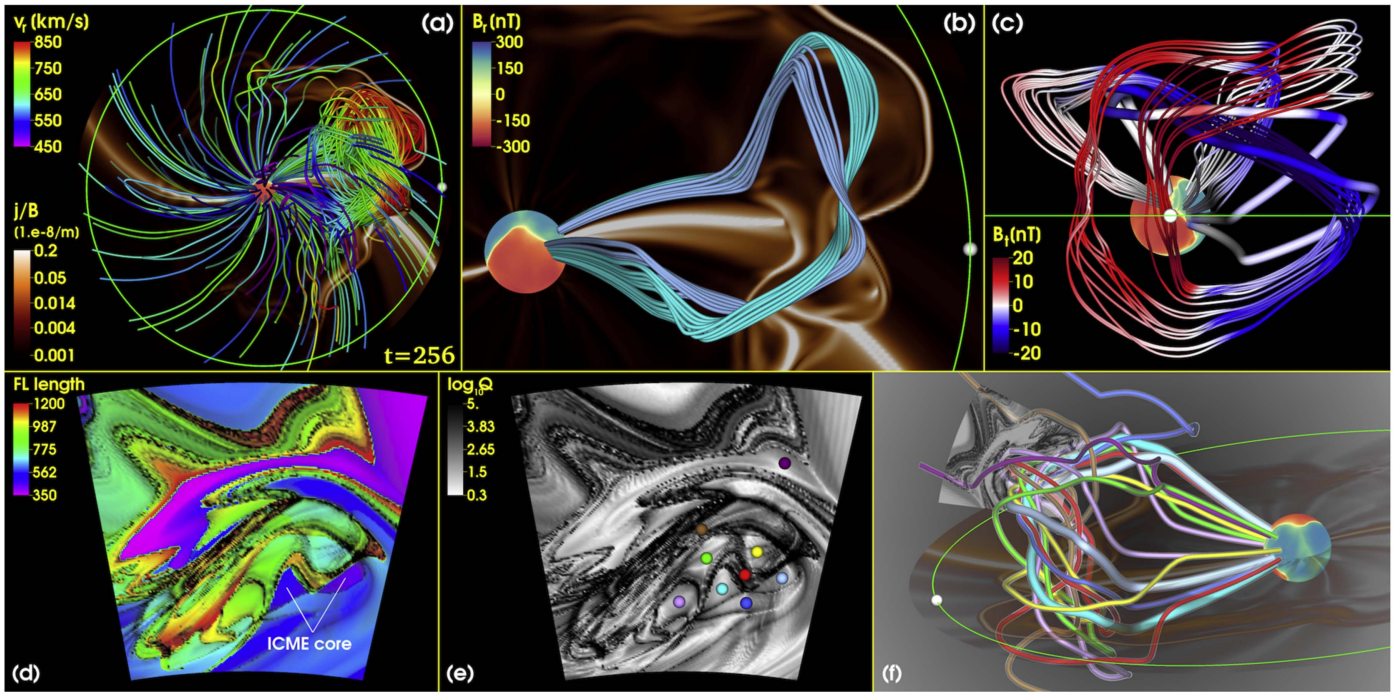
Figure 11. (a) Interplanetary magnetic field and ICME flux rope at $t = 256$. Field lines are colored by v_r; the view is from the north onto the ecliptic plane, which is colored by transparent $|j|/|B|$. Earth's position is marked by a white sphere; the central sphere shows $B_r(r = 20\,R_\odot)$. (b) Close-up view on (a), showing two flux bundles at the core of the flux rope. (c) View from Earth. Field lines are colored by B_θ. Red colors correspond to negative B_Z. The core flux bundles are shown here as tubes; thin field lines show two flux bundles wrapping around them. (d) Vertical plane segment at $\phi = 5.362$, around the location of the flux-rope core, showing $\log Q$ overlaid on the total field line length (in solar radii). (e) Same segment, showing only the Q map. Colored spheres mark the starting points of the field lines shown in (f). (f) Field lines crossing the Q segment. Thick cyan and light-blue field lines show the ICMe core; thinner field lines cross neighboring areas in the Q map.

current ICME flux-rope reconstruction techniques (e.g., Riley et al. 2004; Tappin & Howard 2009).

Figure 11(c) shows field lines colored by the magnitude of B_θ; positive B_θ (red) is approximately in the direction of negative B_z at Earth. The two core flux bundles shown in Figure 11(b) are depicted here as tubes, and two flux bundles that wrap around the core flux are shown as well. It can be seen that the azimuthal field lines in front of the core flux are dominated by negative B_z; their orientation is favorable for reconnection with Earth's magnetic field.

5.3. Synthetic In Situ Measurements

To compare synthetic in situ data extracted from the simulation with actual measurements, we first have to assign a real time to the onset of the simulated eruption. By comparing the early rise phase of the flux rope (Figure 6(a)) with *TRACE* observations of the erupting filament, we associate the simulation time $t = 164$ with 10:10 UT on July 14. The first contact of the simulated ICME with the $r = 215\,R_\odot$ surface (≈ 0.99 au, where the *WIND* and *ACE* spacecraft are located) occurs at $t \approx 259$, about 38.2 hr after the onset of the eruption (see Section 5.4). This time corresponds to 00:20 UT on July 16, which is more than 5 hr after the arrival time of the observed MC (Section 2). The magnetic field signatures associated with the arrival of the modeled ICME at 0.99 au are located $\gtrsim 20°$ west of Earth and are dominated by a positive sign of B_z (see Figure 13(b)), which is opposite to the sign measured by *WIND* and *ACE*.

Synthetic measurements at Earth's position. Figure 12(a) provides a comparison of synthetic in situ measurements at Earth (green curves) with one-hour-averaged OMNI data (blue curves). We choose Earth's position at 02:40 UT on July 16 for

this comparison, which is approximately when the first clear signatures of the simulated ICME core (the MC) appear at $r = 215\,R_\odot$, about 20° north and 5° east of Earth (red curves; see next paragraph). The first clear signal of the modeled ICME appears at Earth's position only more than 9 hr later (due to the strong distortion of the ICME shape; see Section 5.4), much later (almost 18 hr) than the arrival time of the observed MC. The modeled peak velocity at Earth is roughly $750\,\mathrm{km\,s^{-1}}$, about $350\,\mathrm{km\,s^{-1}}$ less than measured for the real MC (note that the higher speed of $\approx 900\,\mathrm{km\,s^{-1}}$ visible in the green curve is associated with the high-speed stream that follows the ICME; see Figure 10(c)). The simulated magnetic field strengths are much weaker than the observed ones as well. While the correct sign of the B_z component is reproduced, the observed rotation of B_z from negative to positive is not. This means that the MC does not pass Earth in the simulation.

Synthetic measurements at the MC's position. Going back to Figure 11(c), we see that the center of the modeled MC (the two tubes outlining the ICME core flux) passes the $r = 215\,R_\odot$ surface north of the ecliptic (by roughly 20°). This was apparently not the case in the real event: while the strong B_x component (see the OMNI data in Figure 12) suggests that the axis of the Bastille Day MC also passed north of Earth, the pattern of the B_z component suggests that the axis was significantly closer to the ecliptic (see also Figures 9 and 10 in Yurchyshyn et al. 2001). To infer how the magnetic field components and the plasma quantities would appear if the center of the modeled MC had passed Earth's position, we add in Figure 12(a) synthetic in situ measurements (red curves) at the approximate location of the MC center, which is 20° north and 5° east of Earth's position (indicated by the circle marked as N20E05 in Figure 13(a)). It can be seen that the synthetic
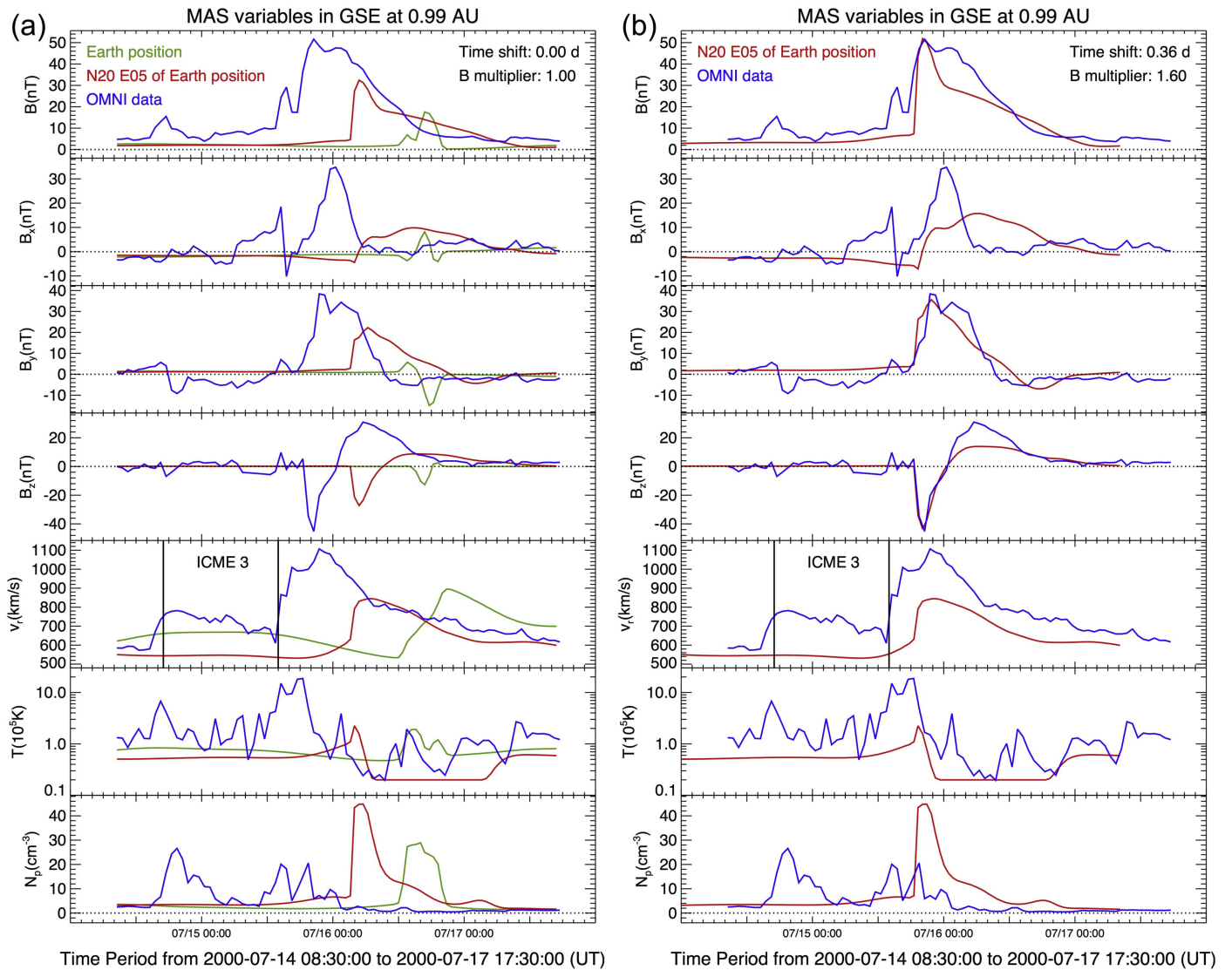
Figure 12. Comparison of real and synthetic in situ data. Blue: one-hour-averaged OMNI data (GSE coordinate system) as provided by CDAWeb. Green: synthetic data at Earth's position (see text for details). Red: simulation data 20° N and 5° E of Earth's position. The vertical lines in the v_r plot indicate a preceding ICME (termed ICME 3 in Smith et al. 2001), which is not present in the simulation. (a) Observed and simulated data, without modification of the simulation data. (b) Matching of the observed and simulated magnetic fields for the MC. To obtain a reasonable match, the simulation time is shifted by 8.5 hr and the magnetic-field components are multiplied by 1.6.

data at this location match the observed ones much better than those extracted at Earth's position: the field strengths are larger, and the time difference between the simulated and the real event is considerably smaller, about 8.5 hr.

To ease the comparison between the model and the real event, we shift the simulation data by 8.5 hr and multiply the magnetic field components by 1.6 so that the peak magnetic field strengths of the model and of the real data match. This is shown in Figure 12(b). It can be seen that the structure of the simulated MC is qualitatively consistent with the MC inferred from the real data: a full rotation of B_z from negative to positive, and B_x, $B_x > 0$ as the spacecraft passes through the left-handed flux rope below its axis. Specifically, the shape of B_z before the sign switches from negative to positive is almost perfectly reproduced after these modifications, without any stretching of the time axis. We can further see that the shock preceding the observed MC by about 5 hr is not present in the simulation; the shock that forms in the low corona during the early phase of the eruption (see Section 4.2) has vanished

(likely due to numerical diffusion) by the time the ejecta reaches $r = 215\,R_\odot$. Figure 12(b) also shows that the modeled peak plasma temperature is more than five times smaller than the real one, while the peak plasma density is more than two times larger. This indicates that too much cold and dense material is lifted upward by the flux rope during the simulated eruption (see Section 4.2).

5.4. ICME Pattern at 1 au

Considering Figure 12(a), it seems surprising that the green and red curves differ that much (particularly in the arrival times of the ICME), given that the transverse distance between the locations at which they were obtained is not particularly large; both locations are well inside the spatial extent of the ICME (Figure 13). The pronounced differences are due to the strong distortion of the ICME shape discussed in Section 5.1. To demonstrate this, we show in Figure 13 the magnetic field
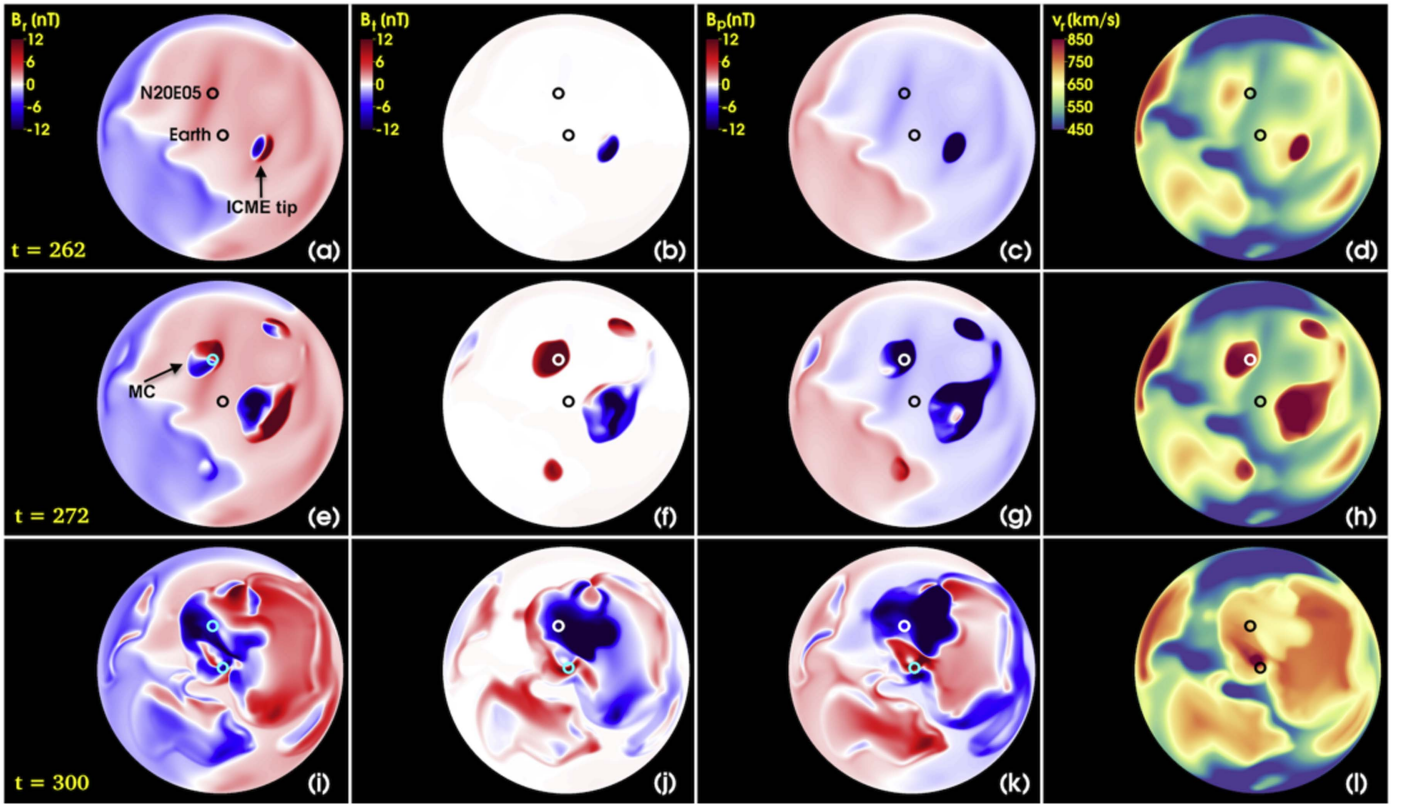
Figure 13. B_r, B_θ, B_ϕ, and v_r on the $r = 215\,R_\odot$ surface at different times in the interplanetary run. The positions at which the green and red curves in Figure 12 were obtained are marked by circles. (a)–(d) About 1 hr after the first encounter of the ICME with the surface. (e)–(h) 4 hr later, when the MC passes through. (i)–(l) Another 11 hr later, when clear ICME signatures have become visible at Earth. The velocity enhancement at Earth's location in (l) corresponds to the arrival of the high-speed stream that trails the ICME (see Figure 10(c)).

components and the radial plasma flow on the $r = 215\,R_\odot$ surface at different times during the passage of the ICME.

Figures 13(a)–(d) show these quantities at $t = 262$ (corresponding to ≈01:30 UT on July 16), about one hour after the first encounter of the ICME with the $r = 215\,R_\odot$ surface. A localized bipolar magnetic structure appears approximately 20° west and 5° south of Earth, corresponding to the ICME tip visible in the equatorial plane in Figure 10(c). The structure is dominated by negative B_θ (positive B_z). Figures 13(e)–(h) show the situation four hours later (≈05:30 UT on July 16), which is approximately when the simulated MC (crossing the surface at the location marked N20E05 in Figure 13(a)) reveals its peak field strength. Several clearly isolated structures are now visible; the ICME appears surprisingly incoherent and inhomogeneous. Note, in particular, the very different orientations of the respective PILs of these structures (Figure 13(e)) and the opposite signs of B_θ (B_Z) of the structures associated with the MC and the ICME tip, respectively (Figure 13(f)). This scattered and inhomogeneous pattern results from the ICME's distortion; the isolated structures outline the "bulges" of the ICME (see Figure 10) crossing the surface. Even another 11.2 hr later (≈16:45 UT on July 16), when the main body of the ICME passes through and the distinct structures have merged into a single one (Figures 13(i)–(l)), the distribution of the quantities remains rather inhomogeneous, reflecting the complex inner structure of the ICME described in Section 5.2. The plasma density and temperature exhibit a similar evolution. We discuss the potential implications of these results in the next section.

6. Summary and Discussion

We presented an MHD simulation of an extreme solar eruption: the "Bastille Day" flare and halo CME that took place on 2000 July 14 in NOAA AR 9077 and produced a very strong geomagnetic storm (Section 2). The simulation was set up using observed magnetograms and a thermodynamic MHD model of the global corona (Section 3.1). A novel ingredient of our simulation, compared to previous Sun-to-Earth simulations of observed events, is the initiation of the eruption from a stable magnetic configuration that was constructed using several instances of the TDm coronal flux-rope model (Section 3.2). Employing such configurations is essential for a realistic modeling of the storage and release of free magnetic energy associated with solar eruptions. The eruption was triggered by imposing converging flows toward the source region's PIL (Section 3.3).

The simulation reproduces the rapid, strong energy release (here about 1.3×10^{33} erg within a few minutes) that is characteristic of extreme eruptions such as the Bastille Day event (Section 4.1). This demonstrates, for the first time, that very impulsive eruptions can be modeled with thermodynamic MHD simulations that start from pre-eruptive configurations in stable magnetic equilibrium. The CME rapidly accelerates to a peak speed of ≈2500 km s^{-1} and produces a shock low in the corona before it has reached $r = 1.5\,R_\odot$ (Section 4.2). The propagation speed of the CME in the outer corona is ≈1500 km s^{-1}, about 200 km s^{-1} less than the observed peak propagation speed. The simulation yields a good agreement with the observed morphologies of the flare arcade and the halo

CME (Section 4.3), and it reproduces the EUV wave and coronal dimmings associated with the eruption (Section 4.4). A second, sympathetic eruption that occurred at the western edge of NOAA AR 9077 a few hours after the main event is also reproduced self-consistently (Section 4.5).

By coupling the coronal thermodynamic MHD simulation to a computationally less expensive heliospheric simulation (Section 3.4), we modeled the interplanetary propagation of the ICME associated with the Bastille Day event to Earth. The ICME shape gets significantly distorted by the ambient solar wind, while no significant deflection of its trajectory can be seen (Section 5.1). We analyzed the magnetic structure of the ICME and found that the overall initial structure of the coronal flux rope (predominantly axial fields at the rope center, surrounded by azimuthal fields) survives during the propagation to 1 au (i.e., the modeled ICME core has properties similar to the MC inferred from the in situ spacecraft measurements). However, the interaction of the ICME flux rope with the solar wind and interplanetary magnetic field introduces a significant amount of complexity to the structure: field lines become highly distorted, the axial flux at the center of the ICME splits into two distinct regions (i.e., a clearly defined single flux-rope axis ceases to exist), and the flux rope is intruded by disconnected flux (Section 5.2).

We then produced synthetic in situ data at 1 au to carry out a direct comparison with the spacecraft measurements (Section 5.3). We found that, while the correct sign of B_z at Earth's location is reproduced in the simulation, the observed rotation of B_z is not. Furthermore, the first clear signatures of the simulated ICME at Earth's location are delayed by almost 18 hr, and the peak field strengths are too low by a factor of about three. The 1 au signatures produced by the core of the simulated ICME (the MC) match the data much better. However, compared to the observed MC, the simulated one has weaker field strengths (by a factor of about 1.6), and it arrives at 1 au about 8.5 hr later (with a speed that is about $250 \, \mathrm{km \, s^{-1}}$ too low) and about $(15\text{--}20)°$ too far to the north; in other words, it misses Earth, unlike the observed MC.

These quantitative differences are not extremely large, given that we used various simplifications, such as a steady-state corona and heliosphere, and did not adjust our initial conditions to exactly match the observed CME speed (as discussed in the Introduction, our approach is to model observed CME properties self-consistently, and our aim here was to test how well the in situ data are reproduced if no such observations are used to set up the simulation). Yet, the differences between the model and the observations are significant in light of the potential application of state-of-the-art MHD simulations for space-weather predictions. Despite these disagreements, our coronal-heliospheric simulation represents a significant advance in the numerical modeling of CMEs and ICMEs, and it is among the most detailed and self-consistent simulations of an observed event all the way from its launch at the Sun to its arrival at Earth. In what follows, we discuss the possible reasons for the discrepancies between the simulation and the real event.

ICME field strengths. The simulated field strengths at 1 au are considerably smaller than the ones measured at Earth. A possible reason for this mismatch could be that the real current-carrying pre-eruptive flux was located at lower atmospheric heights (i.e., at locations of larger field strength) than in our simulation. Since we placed our initial flux rope already very close to the bottom boundary, this would imply that the real pre-eruptive core flux must have had a significantly smaller diameter than our rope. Another, more plausible explanation may be an underestimation of the real field strengths in the MDI LOS magnetogram that was used to model the source region of the eruption, NOAA AR 9077; such underestimates have been described previously by Liu et al. (2007). In this respect, it is interesting to note that a wide range of observatory maps appear to underestimate the interplanetary magnetic flux when incorporated into models or coronal hole detections (Linker et al. 2017), although the reasons for this are uncertain.

CME and ICME speed. Both the simulated CME and MC are $\approx (200\text{--}250) \, \mathrm{km \, s^{-1}}$ slower than observed ones, which leads to a considerable delay of the ejecta's arrival time at 1 au. There may be several reasons for this mismatch. (1) The real ICME was preceded by several consecutive ICMEs that are not included in our simulation. Those may have "preconditioned" the solar wind by means of background density depletion, as has been suggested, for example, for the 2012 July 23 event (Liu et al. 2014; Temmer & Nitta 2015); see also Temmer et al. (2017). (2) The potential underestimation of the real source-region field strengths may yield an underestimation of the free magnetic energy in the model, and hence an eruption that is not impulsive enough to reproduce the observed CME speed. (3) The acceleration of CMEs is governed to a large degree by reconnection that takes place below the CME (e.g., Vršnak 2008). If the reconnection is less efficient in the simulation than in reality, a smaller propagation speed of the CME (and hence of the ICME) may result. (4) Viscous/ resistive dissipation in MHD simulations is larger than in the real solar corona and solar wind and may lead to an artificial slowing of the simulated ejecta.

CME/ICME trajectory deviation. The simulated MC arrives about $(15\text{--}20)°$ too far north compared to the observed one. Again, there may be several reasons for this discrepancy. (1) Our simulation does not include the eruption of a large transequatorial filament that took off almost simultaneously with the Bastille Day event (Wang et al. 2006). An interaction or collision with this event (or with the ICME that preceded the arrival of the Bastille Day MC; Figure 12) may have altered the trajectory of the Bastille Day CME/ICME (e.g., Lugaz et al. 2012; Shen et al. 2012a; Mishra et al. 2017). (2) Asymmetries of the background magnetic field in a CME source region can lead to a nonradial rise of the erupting flux, right from the beginning of the eruption (e.g., Aulanier et al. 2010; Shen et al. 2011; Panasenco et al. 2013; Török et al. 2013; Kay et al. 2015; Liewer et al. 2015; Möstl et al. 2015). A visual comparison of the simulated eruption with the *TRACE* observations indicates that the real CME trajectory was, from the very beginning, directed more southward than in the simulation. As discussed above, strong fields may have been underestimated in the MDI magnetogram we used to model the source region. This may have led to some misrepresentation of the magnetic-field asymmetries, and hence to a somewhat different initial rise direction of the simulated CME. (3) The presence of adjacent coronal holes can lead to in-course changes (deflection) of a CME's trajectory (e.g., Cremades et al. 2006; Gopalswamy et al. 2009; Kilpua et al. 2009; Mohamed et al. 2012; see also Manchester et al. 2017). Due to computational limitations, the flux outside of NOAA AR 9077 is underresolved and strongly smoothed in our simulation (see Section 3.1). Therefore, coronal holes may not

be properly represented in the model. In the real event, they may have deflected the erupting flux rope toward the south. However, it is not clear if that would be a significant effect: strong and fast CMEs like the one associated with the Bastille Day eruption may not experience significant deflection, and the available satellite images do not indicate the presence of pronounced coronal holes north of NOAA AR 9077.

An important result of our investigation is that the simulated ICME arrives at 1 au with a very scattered and inhomogeneous pattern of the magnetic field and plasma quantities (Section 5.4; see Figure 13). Specifically, the field strength, the sign of B_Z, and the plasma flow speed vary considerably over the region occupied by the ICME. This pattern likely results from the combined action of internal reconfigurations of the flux rope, its nonuniform expansion, and from its distortion by gradients in the solar wind speed. During solar minima, when the solar wind has a relatively simple bimodal structure, a dominant concave distortion can be expected, at least for low-latitude ICMEs that travel along the heliospheric current sheet (e.g., Odstrcil & Pizzo 1999; Manchester et al. 2004; Savani et al. 2010). During solar maxima, when the structure of the wind is intricate and gradients between regions of fast and slow wind are smaller (Riley et al. 2003), ICME distortions will be more complex but probably less pronounced. However, strong additional (convex) distortions may develop for events in which parts of the ejecta travel significantly faster than the background solar wind, as is the case in our simulation.

If the pattern shown in Figure 13 is indeed representative of real (fast and complex) events, this means that a reasonably accurate forecast of ICME or MC signatures observed at Earth by means of MHD simulations remains very challenging. Inaccuracies in the CME/ICME trajectory (as in our simulation) of just a few degrees may lead to incorrect predictions of the magnetic field strength, the sign of B_z, the speed of the ejecta, and its arrival time.

Thus, from both a scientific and a forecasting perspective, the MHD modeling of solar eruptions requires further development. As discussed in the Introduction, we believe that initiating CMEs slowly from pre-eruptive configurations in stable magnetic equilibrium is one important step toward more realism and accuracy. The technique presented in Section 3.2 constitutes a significant step forward, but for complex pre-eruptive configurations, it may require a significant number of trial-and-error attempts, as several instances of the TDm model will be necessary to cover an elongated and highly curved eruptive PIL. To overcome this limitation, we have recently developed a new analytical flux-rope model, which allows one to use a single flux rope of arbitrary shape for the construction of stable pre-eruptive equilibrium configurations (Titov et al. 2018).

The development of stable pre-eruptive configurations could benefit also from incorporating NLFFF extrapolations or models (e.g., Schrijver et al. 2008b; Savcheva & van Ballegooijen 2009), as recently demonstrated by Amari et al. (2014, 2018), or information from flux-emergence simulations that model the formation of such configurations (e.g., Archontis & Török 2008; Cheung et al. 2010; Fang et al. 2012; Leake et al. 2013; Toriumi et al. 2014; Török et al. 2014). First steps in the latter direction have been undertaken by, for example, Roussev et al. (2012) and Török et al. (2016), who used flux-emergence models to drive simulations of coronal eruptions, albeit so far only for idealized magnetic configurations. Also,

observed photospheric flows should be included to provide a more realistic description of the energy build-up prior to eruptions and of their initiation (e.g., Jiang et al. 2016). Furthermore, a more advanced and realistic modeling of the environment in which CMEs and ICMEs travel should be tackled. To this end, time-dependent, continuously updated MHD models of the global corona and interplanetary space need to be developed, similar to what is already done in NLFFF flux-transport models (see, e.g., Mackay & Yeates 2012). Future models must also be able to simulate several eruptions simultaneously, to account for the interaction of CMEs/ICMEs with one another.

Despite their current limitations, state-of-the-art simulations such as the one presented here provide an excellent tool for scientific investigations of various aspects of solar eruptions, in a close-to-realistic magnetic-field and plasma environment. Here we studied, for example, the evolution of the EUV wave and the coronal dimmings associated with the Bastille Day eruption and the triggering mechanism of the second eruption to a degree of detail that would not have been possible by using observations or idealized simulations. Our simulation data are currently used to evaluate uncertainties in coronal electron temperature and speed measurements (Reginald et al.; article under revision), to benchmark image-based CME reconstruction techniques (e.g., Wood et al. 2017), and to model the acceleration and propagation of energetic particles (as described for a different simulation in Schwadron et al. 2014). Other intended applications have been mentioned throughout the text. We encourage interested researchers to contact us if they would like to use our simulation data for complementary investigations.

Appendix A
The MAS Thermodynamic MHD Model

The numerical code MAS employed in this article integrates the standard viscous and resistive one-fluid MHD equations in 3D spherical coordinates. For the coronal simulation described in Sections 3.1–3.3 and 4, the so-called "thermodynamic MHD model" was used, in which the standard equations are extended to include parallel electron thermal conduction, radiative losses, and parameterized coronal heating. The MAS thermodynamic MHD model has been used extensively for simulating the global corona and solar wind (e.g., Mikić et al. 1999, 2007; Lionello et al. 2001, 2009; Downs et al. 2013; Linker et al. 2017; Titov et al. 2017) and eruptive phenomena such as soft X-ray jets (Lionello et al. 2016; Török et al. 2016) and CMEs (e.g., Linker et al. 2001, 2003; Mikić et al. 2013b). In this article, we use a version of the model in which the solar wind is accelerated with Alfvén waves using a Wentzel–Kramers–Brillouin (WKB) approximation (Jacques 1977). A more sophisticated wave-acceleration model is under development (Lionello et al. 2014; Downs et al. 2016). In the version used

here, the governing equations take the following form:

$$\frac{\partial \boldsymbol{A}}{\partial t} = \boldsymbol{v} \times (\nabla \times \boldsymbol{A}) - \frac{c^2\,\eta}{4\,\pi}\,\nabla \times \nabla \times \boldsymbol{A}, \qquad (1)$$

$$\frac{\partial \rho}{\partial t} = -\nabla \cdot (\rho\,\boldsymbol{v}), \qquad (2)$$

$$\begin{aligned}
\frac{\partial T}{\partial t} = &-\nabla \cdot (T\boldsymbol{v}) - (\gamma - 2)(T\,\nabla \cdot \boldsymbol{v}) \\
&- \frac{1}{2}\,\nabla \cdot (f_{\mathrm{nc}}(r)\,T\,\boldsymbol{v}\,\hat{\boldsymbol{b}}\hat{\boldsymbol{b}}) \\
&+ \frac{(\gamma-1)}{2\,k}\frac{m_p}{\rho}\Bigg[\nabla \cdot (\beta_{\mathrm{Tcut}}(T)f_c(r)\kappa_0\,T^{5/2}\,\hat{\boldsymbol{b}}\hat{\boldsymbol{b}} \cdot \nabla T) \\
&- \frac{\rho^2}{m_p^2}\,\frac{Q(T)}{\beta_{\mathrm{Tcut}}(T)} + H\Bigg],
\end{aligned}$$
$$(3)$$

$$\begin{aligned}
\frac{\partial \boldsymbol{v}}{\partial t} = &-\boldsymbol{v} \cdot \nabla\,\boldsymbol{v} \\
&+ \frac{1}{\rho}\Bigg[\frac{1}{c}\boldsymbol{J} \times \boldsymbol{B} - \nabla p - \nabla\left(\frac{\epsilon_+ + \epsilon_-}{2}\right) + \rho\,\boldsymbol{g}\Bigg] \\
&+ \frac{1}{\rho}\,\nabla \cdot (\nu\rho\nabla\boldsymbol{v}) + \frac{1}{\rho}\,\nabla \cdot \left(S\,\rho\,\nabla\frac{\partial \boldsymbol{v}}{\partial t}\right),
\end{aligned}$$
$$(4)$$

$$\frac{\partial \epsilon_+}{\partial t} = -\nabla \cdot (\epsilon_+[\boldsymbol{v} + v_{\mathrm{A}}\,\hat{\boldsymbol{b}}]) - \frac{1}{2}\,\epsilon_+\,\nabla \cdot \boldsymbol{v}, \qquad (5)$$

$$\frac{\partial \epsilon_-}{\partial t} = -\nabla \cdot (\epsilon_-[\boldsymbol{v} - v_{\mathrm{A}}\,\hat{\boldsymbol{b}}]) - \frac{1}{2}\,\epsilon_-\,\nabla \cdot \boldsymbol{v}, \qquad (6)$$

where $\boldsymbol{A}$ is the magnetic vector potential, $\boldsymbol{B} = \nabla \times \boldsymbol{A}$ is the magnetic field, $\boldsymbol{J} = \frac{c}{4\pi}\nabla \times \boldsymbol{B}$ is the current density, ρ is the plasma density, T is the temperature, $p = 2\,kT\,\rho/m_p$ is the plasma pressure, $\boldsymbol{v}$ is the plasma velocity, $\hat{\boldsymbol{b}} = |\boldsymbol{B}|/\boldsymbol{B}$ is the direction of the magnetic field, c is the speed of light, $\gamma = 5/3$ is the adiabatic index, m_p is the proton mass, k is Boltzmann's constant, κ_0 is the coefficient of the classical Spitzer thermal conductivity, $f_c(r) = 0.5(1 - \tanh[(r - 10\,R_\odot)/0.5\,R_\odot])$ is a profile that limits the radial extent within which collisional (Spitzer's law) thermal conduction is active, $f_{\mathrm{nc}}(r) = 1 - f_c(r)$ is the equivalent profile for collisionless thermal conduction, $Q(T)$ is the radiative loss function, H is the coronal heating term that typically consists of a sum of empirical heating functions (Lionello et al. 2009), $v_{\mathrm{A}} = \sqrt{|\boldsymbol{B}|^2/4\,\pi\,\rho}$ is the Alfvén-wave speed, and $\boldsymbol{g} = -g_0\,R_\odot^2\,\hat{\boldsymbol{r}}/r^2$ is the gravitational force. Note that joule heating, ηJ^2, is not included in Equation (3). While it is implemented in MAS, we switch it off in our simulation, otherwise the insertion of the current-carrying flux rope into the background corona (Section 3.2) would lead to an instantaneous, unphysical temperature increase of the rope. The last expression in Equation (4) is a semi-implicit term that is added to the equations to stabilize the algorithm for time steps larger than the fast magnetosonic wave limit (Lionello et al. 1999; Caplan et al. 2017). Equations (5) and (6) are the WKB approximation for Alfvén-wave pressure advance (Mikić et al. 1999), where

ϵ_+ and ϵ_- are the forward and backward Alfvén-wave energy densities.

The electron density at the lower boundary is set to a fixed value that is large enough to avoid evaporation of the model chromosphere in regions of strong heating (see Lionello et al. 2009 for a detailed discussion). In the simulation, we use $n_e = 2 \times 10^{12}\,\mathrm{cm}^{-3}$, which is roughly consistent with values typically estimated for the upper chromosphere. The function $\beta_{\mathrm{Tcut}}(T)$ is a cut-off function that serves to broaden the transition region; $\beta_{\mathrm{Tcut}} = (T/T_{\mathrm{cut}})^{5/2}$ for $T < T_{\mathrm{cut}}$ and $\beta_{\mathrm{Tcut}} = 1$ for $T \geqslant T_{\mathrm{cut}}$. Applying this function allows one to increase the width of the transition region (i.e., its spatial resolution) with a minimal effect on the global coronal solution (Lionello et al. 2009; Mikić et al. 2013a). We use $T_{\mathrm{cut}} = 5 \times 10^5\,\mathrm{K}$ in the simulation. The resistivity, η, and the kinematic viscosity, ν, are set such that the corresponding diffusion times are $\tau_\eta = (4\pi\,R_\odot^2)/(\eta c^2) \approx 4 \times 10^5\,\mathrm{hr}$ and $\tau_\nu = R_\odot^2/\nu \approx 80\,\mathrm{hr}$, respectively, much larger than the Alfvén time of ≈ 24 minutes.

For the interplanetary simulation described in Sections 3.4 and 5, thermal conduction, radiative losses, and coronal heating are neglected, γ is set to $3/2$, and a smaller kinematic viscosity, corresponding to $\tau_\nu \approx 400\,\mathrm{hr}$, is used. The characteristic form of the MHD equations is employed for both simulations to specify the boundary conditions at the radial boundaries (see Linker & Mikić 1997 for details).

Appendix B
Analysis of the Magnetic Field Using the Squashing Factor

Separatrix surfaces (SSs) and quasi-separatrix layers (QSLs) are, respectively, topological and geometrical features that fully or partly partition magnetic configurations into different flux systems (e.g., Priest 2014). They can be identified by computing appropriate maps of the so-called squashing factor (or squashing degree), Q (Titov et al. 2002). In essence, Q is a measure of how elliptical an infinitesimal circular region of one polarity becomes when mapped along field lines to its conjugate footprint. Its minimum value, $Q = 2$, corresponds to the mapped footprint remaining circular. Larger values of Q describe how fanned out a field-line bundle becomes from one end to the other. Regions with $Q \gg 2$ determine QSLs. In the limit $Q \to \infty$, occurring at field lines that thread either a magnetic null or a bald patch, the magnetic surface spanned by these field lines becomes an SS. In numerical studies, such a surface appears as unresolved spikes of Q, so that both true SSs and QSLs, as well as their hybrids, are detected by computing Q distributions. Initially, Q was defined for closed field lines, but it can be computed for open field lines as well (Titov 2007; Titov et al. 2008). Overall, Q becomes very large or infinite at locations where the magnetic structure experiences an abrupt change (e.g., Savcheva et al. 2012; Titov et al. 2012, 2017).

By construction, Q is invariant to the direction of the field-line mapping (Titov et al. 2002). Therefore, its value at conjugate foot points of a field line at a boundary can be assigned to any point of the field line. Thus, by mapping Q along field lines from a boundary (e.g., the inner boundary of our simulation domain) to cross sections of interest, it becomes possible to visualize QSLs at any plane in the volume (Titov et al. 2008; Pariat & Démoulin 2012; Liu et al. 2016). Such visualization significantly helps to interpret the structure of complex magnetic fields, and it was used in our analysis of the ICME flux rope shown in Figure 11. For complex Q maps such

as the one shown in Figure 11(e), it is useful to color the map by the field line length, L, which yields an "L map," as shown in Figure 11(d). The L map aids the interpretation, since distinct segments of the same (or very similar) color typically outline flux bundles that cross the Q map two times or more (or conjugate footprints of coronal flux bundles if the Q and L maps are calculated at the photosphere).

ORCID iDs

Tibor Török ⬤ https://orcid.org/0000-0003-3843-3242
Cooper Downs ⬤ https://orcid.org/0000-0003-1759-4354
R. Lionello ⬤ https://orcid.org/0000-0001-9231-045X
Viacheslav S. Titov ⬤ https://orcid.org/0000-0001-7053-4081
Zoran Mikić ⬤ https://orcid.org/0000-0002-3164-930X
Ronald M. Caplan ⬤ https://orcid.org/0000-0002-2633-4290

References

Aly, J. J. 1991, ApJL, 375, L61
Aly, J. J., & Amari, T. 2007, GApFD, 101, 249
Amari, T., Aly, J. J., Mikic, Z., & Linker, J. 2007, ApJL, 671, L189
Amari, T., Canou, A., & Aly, J.-J. 2014, Natur, 514, 465
Amari, T., Canou, A., Aly, J.-J., Delyon, F., & Alauzet, F. 2018, Natur, 554, 211EP
Amari, T., Luciani, J. F., Aly, J. J., Mikic, Z., & Linker, J. 2003, ApJ, 585, 1073
Amari, T., Luciani, J. F., Aly, J. J., & Tagger, M. 1996, ApJL, 466, L39
Amari, T., Luciani, J. F., Mikic, Z., & Linker, J. 2000, ApJL, 529, L49
Andrews, M. D. 2001, SoPh, 204, 179
Antiochos, S. K., DeVore, C. R., & Klimchuk, J. A. 1999, ApJ, 510, 485
Archontis, V., & Török, T. 2008, A&A, 492, L35
Aulanier, G. 2014, in IAU Symp. 300, Nature of Prominences and their Role in Space Weather, ed. B. Schmieder, J.-M. Malherbe, & S. T. Wu (Cambridge: Cambridge Univ. Press), 184
Aulanier, G., Török, T., Démoulin, P., & DeLuca, E. E. 2010, ApJ, 708, 314
Baker, D. N., & Lanzerotti, L. J. 2016, SpWea, 14, 528
Bieber, J. W., Dröge, W., Evenson, P. A., et al. 2002, ApJ, 567, 622
Birn, J., Fletcher, L., Hesse, M., & Neukirch, T. 2009, ApJ, 695, 1151
Brueckner, G. E., Howard, R. A., Koomen, M. J., et al. 1995, SoPh, 162, 357
Caplan, R. M., Mikić, Z., Linker, J. A., & Lionello, R. 2017, Journal of Physics Conference Series, 837, 012016
Chen, P. F. 2011, LRSP, 8, 1
Chen, P. F., & Shibata, K. 2000, ApJ, 545, 524
Cheng, X., Zhang, J., Liu, Y., & Ding, M. D. 2011, ApJL, 732, L25
Chertok, I. M., & Grechnev, V. V. 2005, SoPh, 229, 95
Cheung, M. C. M., Rempel, M., Title, A. M., & Schüssler, M. 2010, ApJ, 720, 233
Cohen, O., Attrill, G. D. R., Manchester, W. B., IV, & Wills-Davey, M. J. 2009, ApJ, 705, 587
Cremades, H., Bothmer, V., & Tripathi, D. 2006, AdSpR, 38, 461
Delaboudinière, J.-P., Artzner, G. E., Brunaud, J., et al. 1995, SoPh, 162, 291
Démoulin, P. 2008, AnGeo, 26, 3113
DeVore, C. R., & Antiochos, S. K. 2005, ApJ, 628, 1031
Downs, C., Linker, J. A., Mikić, Z., et al. 2013, Sci, 340, 1196
Downs, C., Lionello, R., Mikić, Z., Linker, J. A., & Velli, M. 2016, ApJ, 832, 180
Downs, C., Roussev, I. I., van der Holst, B., et al. 2010, ApJ, 712, 1219
Downs, C., Roussev, I. I., van der Holst, B., et al. 2011, ApJ, 728, 2
Downs, C., Roussev, I. I., van der Holst, B., Lugaz, N., & Sokolov, I. V. 2012, ApJ, 750, 134
Fan, Y. 2016, ApJ, 824, 93
Fan, Y., & Gibson, S. E. 2003, ApJL, 589, L105
Fang, F., Manchester, W., IV, Abbett, W. P., & van der Holst, B. 2012, ApJ, 754, 15
Fenrich, F. R., & Luhmann, J. G. 1998, GeoRL, 25, 2999
Forbes, T. G. 1990, JGR, 95, 11919
Forbes, T. G., Linker, J. A., Chen, J., et al. 2006, SSRv, 123, 251
Gopalswamy, N. 2006, JApA, 27, 243
Gopalswamy, N., Akiyama, S., Yashiro, S., Michalek, G., & Lepping, R. P. 2008, JASTP, 70, 245
Gopalswamy, N., Akiyama, S., Yashiro, S., & Xie, H. 2017, arXiv:1705.08912
Gopalswamy, N., Mäkelä, P., Xie, H., Akiyama, S., & Yashiro, S. 2009, JGRA, 114, A00A22

Green, L. M., Török, T., Vršnak, B., Manchester, W., & Veronig, A. 2018, SSRv, 214, 46
Handy, B. N., Acton, L. W., Kankelborg, C. C., et al. 1999, SoPh, 187, 229
Hu, Y. Q. 2004, ApJ, 607, 1032
Jacques, S. A. 1977, ApJ, 215, 942
Jiang, C., Wu, S. T., Feng, X., & Hu, Q. 2016, NatCo, 7, 11522
Jin, M., Manchester, W. B., van der Holst, B., et al. 2013, ApJ, 773, 50
Jin, M., Manchester, W. B., van der Holst, B., et al. 2017a, ApJ, 834, 172
Jin, M., Manchester, W. B., van der Holst, B., et al. 2017b, ApJ, 834, 173
Jin, M., Schrijver, C. J., Cheung, M. C. M., et al. 2016, ApJ, 820, 16
Joshi, N. C., Schmieder, B., Magara, T., Guo, Y., & Aulanier, G. 2016, ApJ, 820, 126
Karpen, J. T., Antiochos, S. K., & DeVore, C. R. 2012, ApJ, 760, 81
Kay, C., Opher, M., & Evans, R. M. 2015, ApJ, 805, 168
Kilpua, E. K. J., Pomoell, J., Vourlidas, A., et al. 2009, AnGeo, 27, 4491
Kliem, B., Linton, M. G., Török, T., & Karlický, M. 2010, SoPh, 266, 91
Kliem, B., Su, Y. N., van Ballegooijen, A. A., & DeLuca, E. E. 2013, ApJ, 779, 129
Kliem, B., & Török, T. 2006, PhRvL, 96, 255002
Kliem, B., Török, T., & Thompson, W. T. 2012, SoPh, 281, 137
Kusano, K., Bamba, Y., Yamamoto, T. T., et al. 2012, ApJ, 760, 31
Kusano, K., Maeshiro, T., Yokoyama, T., & Sakurai, T. 2004, ApJ, 610, 537
Leake, J. E., Linton, M. G., & Török, T. 2013, ApJ, 778, 99
Lemen, J. R., Title, A. M., Akin, D. J., et al. 2012, SoPh, 275, 17
Lepping, R. P., Acūna, M. H., Burlaga, L. F., et al. 1995, SSRv, 71, 207
Lepping, R. P., Berdichevsky, D. B., Burlaga, L. F., et al. 2001, SoPh, 204, 285
Liewer, P., Panasenco, O., Vourlidas, A., & Colaninno, R. 2015, SoPh, 290, 3343
Lin, R. P., Anderson, K. A., Ashford, S., et al. 1995, SSRv, 71, 125
Linker, J., Török, T., Downs, C., et al. 2016, in AIP Conf. Ser. 1720 (Melville, NY: AIP), 020002
Linker, J. A., Caplan, R. M., Downs, C., et al. 2017, ApJ, 848, 70
Linker, J. A., Lionello, R., Mikić, Z., & Amari, T. 2001, JGR, 106, 25165
Linker, J. A., & Mikić, Z. 1997, in Coronal Mass Ejections, ed. N. Crooker, J. Joselyn, & J. Feynman (Washington, DC: AGU), 269
Linker, J. A., Mikić, Z., Lionello, R., et al. 2003, PhPl, 10, 1971
Linker, J. A., Mikić, Z., Riley, P., et al. 2013, in AIP Conf. Proc. 1539, Solar Wind 13: Proc. Thirteenth Int. Solar Wind Conf. (Melville, NY: AIP), 26
Lionello, R., Downs, C., Linker, J. A., et al. 2013, ApJ, 777, 76
Lionello, R., Linker, J. A., & Mikić, Z. 2001, ApJ, 546, 542
Lionello, R., Linker, J. A., & Mikić, Z. 2009, ApJ, 690, 902
Lionello, R., Mikić, Z., & Linker, J. A. 1999, JCoPh, 152, 346
Lionello, R., Török, T., Titov, V. S., et al. 2016, ApJL, 831, L2
Lionello, R., Velli, M., Downs, C., et al. 2014, ApJ, 784, 120
Liu, R., Alexander, D., & Gilbert, H. R. 2009, ApJ, 691, 1079
Liu, R., Kliem, B., Titov, V. S., et al. 2016, ApJ, 818, 148
Liu, R., Kliem, B., Török, T., et al. 2012, ApJ, 756, 59
Liu, Y., Norton, A. A., & Scherrer, P. H. 2007, SoPh, 241, 185
Liu, Y. D., Luhmann, J. G., Kajdič, P., et al. 2014, NatCo, 5, 3481
Lugaz, N., Downs, C., Shibata, K., et al. 2011, ApJ, 738, 127
Lugaz, N., Farrugia, C. J., Davies, J. A., et al. 2012, ApJ, 759, 68
Lugaz, N., Manchester, W. B., IV, Roussev, I. I., Tóth, G., & Gombosi, T. I. 2007, ApJ, 659, 788
Lugaz, N., Vourlidas, A., Roussev, I. I., & Morgan, H. 2009, SoPh, 256, 269
Lynch, B. J., & Edmondson, J. K. 2013, ApJ, 764, 87
Lynch, B. J., Gruesbeck, J. R., Zurbuchen, T. H., & Antiochos, S. K. 2005, JGRA, 110, 8107
Mackay, D. H., & Yeates, A. R. 2012, LRSP, 9, 6
Manchester, W., Kilpua, E. K. J., Liu, Y. D., et al. 2017, SSRv, 212, 1159
Manchester, W. B., Gombosi, T. I., Roussev, I., et al. 2004, JGRA, 109, 2107
Manchester, W. B., IV, van der Holst, B., & Lavraud, B. 2014, PPCF, 56, 064006
Manchester, W. B., IV, van der Holst, B., Tóth, G., & Gombosi, T. I. 2012, ApJ, 756, 81
Manchester, W. B., IV, Vourlidas, A., Tóth, G., et al. 2008, ApJ, 684, 1448
Merkin, V. G., Lionello, R., Lyon, J. G., et al. 2016, ApJ, 831, 23
Messerotti, M., Zuccarello, F., Guglielmino, S. L., et al. 2009, SSRv, 147, 121
Mikić, Z., & Linker, J. A. 1994, ApJ, 430, 898
Mikić, Z., Linker, J. A., Lionello, R., Riley, P., & Titov, V. S. 2007, in ASP Conf. Ser. 370, Solar and Stellar Physics Through Eclipses, ed. O. Demircan, S. O. Selam & B. Albayrak (San Francisco, CA: ASP), 299
Mikić, Z., Linker, J. A., Schnack, D. D., Lionello, R., & Tarditi, A. 1999, PhPl, 6, 2217
Mikić, Z., Lionello, R., Mok, Y., Linker, J. A., & Winebarger, A. R. 2013a, ApJ, 773, 94

Mikić, Z., Török, T., Titov, V., et al. 2013b, in AIP Conf. Proc. 1539, Solar Wind 13: Proc. Thirteenth Int. Solar Wind Conf. (Melville, NY: AIP), 42
Mishra, W., Wang, Y., Srivastava, N., & Shen, C. 2017, ApJS, 232, 5
Mohamed, A. A., Gopalswamy, N., Yashiro, S., et al. 2012, JGRA, 117, A01103
Mok, Y., Mikić, Z., Lionello, R., Downs, C., & Linker, J. A. 2016, ApJ, 817, 15
Mok, Y., Mikić, Z., Lionello, R., & Linker, J. A. 2005, ApJ, 621, 1098
Möstl, C., Rollett, T., Frahm, R. A., et al. 2015, NatCo, 6, 7135
Nitta, N. V., Schrijver, C. J., Title, A. M., & Liu, W. 2013, ApJ, 776, 58
Odstrcil, D., & Pizzo, V. J. 1999, JGR, 104, 28225
Odstrcil, D., Pizzo, V. J., & Arge, C. N. 2005, JGRA, 110, A02106
Owens, M. J. 2006, JGRA, 111, A12109
Panasenco, O., Martin, S. F., Velli, M., & Vourlidas, A. 2013, SoPh, 287, 391
Panasenco, O., & Velli, M. 2012, in American Astronomical Society Meeting Abstracts, 220, 202.12
Pariat, E., & Démoulin, P. 2012, A&A, 541, A78
Peng, Z., & Hu, Y. 2007, ApJ, 668, 513
Pesnell, W. D., Thompson, B. J., & Chamberlin, P. C. 2012, SoPh, 275, 3
Priest, E. 2014, Magnetohydrodynamics of the Sun (Cambridge: Cambridge Univ. Press)
Reeves, K. K., Linker, J. A., Mikić, Z., & Forbes, T. G. 2010, ApJ, 721, 1547
Richardson, I. G., & Cane, H. V. 2010, SoPh, 264, 189
Riley, P., Linker, J. A., Lionello, R., et al. 2004, JASTP, 66, 1321
Riley, P., Mikic, Z., & Linker, J. A. 2003, AnGeo, 21, 1347
Roussev, I. I., Forbes, T. G., Gombosi, T. I., et al. 2003, ApJL, 588, L45
Roussev, I. I., Galsgaard, K., Downs, C., et al. 2012, NatPh, 8, 845
Roussev, I. I., Lugaz, N., & Sokolov, I. V. 2007, ApJL, 668, L87
Savani, N. P., Owens, M. J., Rouillard, A. P., Forsyth, R. J., & Davies, J. A. 2010, ApJL, 714, L128
Savcheva, A., & van Ballegooijen, A. 2009, ApJ, 703, 1766
Savcheva, A. S., van Ballegooijen, A. A., & DeLuca, E. E. 2012, ApJ, 744, 78
Scherrer, P. H., Bogart, R. S., Bush, R. I., et al. 1995, SoPh, 162, 129
Schmidt, J. M., & Ofman, L. 2010, ApJ, 713, 1008
Schrijver, C. J., De Rosa, M. L., Metcalf, T., et al. 2008b, ApJ, 675, 1637
Schrijver, C. J., Elmore, C., Kliem, B., Török, T., & Title, A. M. 2008a, ApJ, 674, 586
Schrijver, C. J., & Title, A. M. 2011, JGRA, 116, A04108
Schwadron, N. A., Gorby, M., Török, T., et al. 2014, SpWea, 12, 323
Schwadron, N. A., Lee, M. A., Gorby, M., et al. 2015, ApJ, 810, 97
Shafranov, V. D. 1966, RvPP, 2, 103
Shen, C., Wang, Y., Gui, B., Ye, P., & Wang, S. 2011, SoPh, 269, 389
Shen, C., Wang, Y., Wang, S., et al. 2012a, NatPh, 8, 923
Shen, F., Shen, C., Zhang, J., et al. 2014, JGRA, 119, 7128
Shen, Y., Liu, Y., & Su, J. 2012b, ApJ, 750, 12
Shiota, D., & Kataoka, R. 2016, SpWea, 14, 56
Siscoe, G., & Schwenn, R. 2006, SSRv, 123, 453
Smith, C. W., Ness, N. F., Burlaga, L. F., et al. 2001, SoPh, 204, 227
Sokolov, I. V., van der Holst, B., Oran, R., et al. 2013, ApJ, 764, 23
Srivastava, N., & Venkatakrishnan, P. 2004, JGRA, 109, A10103
Stone, E. C., Frandsen, A. M., Mewaldt, R. A., et al. 1998, SSRv, 86, 1
Sturrock, P. A. 1991, ApJ, 380, 655
Tappin, S. J., & Howard, T. A. 2009, SSRv, 147, 55
Tassev, S., & Savcheva, A. 2017, ApJ, 840, 89

Temmer, M., & Nitta, N. V. 2015, SoPh, 290, 919
Temmer, M., Reiss, M. A., Nikolic, L., Hofmeister, S. J., & Veronig, A. M. 2017, ApJ, 835, 141
Thompson, W. T., Kliem, B., & Török, T. 2012, SoPh, 276, 241
Titov, V. S. 2007, ApJ, 660, 863
Titov, V. S., & Démoulin, P. 1999, A&A, 351, 707
Titov, V. S., Downs, C., Mikić, Z., et al. 2018, ApJL, 852, L21
Titov, V. S., Hornig, G., & Démoulin, P. 2002, JGRA, 107, 1164
Titov, V. S., Mikic, Z., Linker, J. A., & Lionello, R. 2008, ApJ, 675, 1614
Titov, V. S., Mikic, Z., Török, T., Linker, J. A., & Panasenco, O. 2012, ApJ, 759, 70
Titov, V. S., Mikić, Z., Török, T., Linker, J. A., & Panasenco, O. 2017, ApJ, 845, 141
Titov, V. S., Török, T., Mikic, Z., & Linker, J. A. 2014, ApJ, 790, 163
Toriumi, S., Iida, Y., Kusano, K., Bamba, Y., & Imada, S. 2014, SoPh, 289, 3351
Török, T., Berger, M. A., & Kliem, B. 2010, A&A, 516, A49
Török, T., & Kliem, B. 2005, ApJL, 630, L97
Török, T., & Kliem, B. 2007, AN, 328, 743
Török, T., Kliem, B., & Titov, V. S. 2004, A&A, 413, L27
Török, T., Leake, J. E., Titov, V. S., et al. 2014, ApJL, 782, L10
Török, T., Lionello, R., Titov, V. S., et al. 2016, in ASP Conf. Ser. 504, Coimbra Solar Physics Meeting: Ground-based Solar Observations in the Space Instrumentation Era, ed. I. Dorotovic, C. E. Dorotovic, & M. Temmer (San Francisco, CA: ASP), 185
Török, T., Panasenco, O., Titov, V. S., et al. 2011, ApJL, 739, L63
Török, T., Temmer, M., Valori, G., et al. 2013, SoPh, 286, 453
Tóth, G., De Zeeuw, D. L., Gombosi, T. I., et al. 2007, SpWea, 5, 6003
Tsuneta, S., Acton, L., Bruner, M., et al. 1991, SoPh, 136, 37
van Ballegooijen, A. A. 2004, ApJ, 612, 519
van der Holst, B., Manchester, W. B., IV, Frazin, R. A., et al. 2010, ApJ, 725, 1373
van der Holst, B., Sokolov, I. V., Meng, X., et al. 2014, ApJ, 782, 81
van Driel-Gesztelyi, L., Baker, D., Török, T., et al. 2014, ApJ, 788, 85
Vršnak, B. 2008, AnGeo, 26, 3089
Wang, C., Richardson, J. D., & Burlaga, L. 2001, SoPh, 204, 413
Wang, H., Shen, C., & Lin, J. 2009, ApJ, 700, 1716
Wang, J.-X., Zhou, G.-P., Wen, Y.-Y., et al. 2006, ChJAA, 6, 247
Wang, Y., Shen, C., Wang, S., & Ye, P. 2004, SoPh, 222, 329
Wang, Y. M., Ye, P. Z., Wang, S., Zhou, G. P., & Wang, J. X. 2002, JGRA, 107, 1340
Warmuth, A. 2015, LRSP, 12, 3
Wolfson, R., & Low, B. C. 1992, ApJ, 391, 353
Wood, B. E., Wu, C.-C., Lepping, R. P., et al. 2017, ApJS, 229, 29
Xia, C., Keppens, R., & Guo, Y. 2014, ApJ, 780, 130
Yang, J., Jiang, Y., Zheng, R., et al. 2012, ApJ, 745, 9
Yokoyama, T., & Shibata, K. 2001, ApJ, 549, 1160
Yurchyshyn, V. B., Wang, H., Goode, P. R., & Deng, Y. 2001, ApJ, 563, 381
Zhang, H. 2002, MNRAS, 332, 500
Zhang, J., Wang, J., Deng, Y., & Wu, D. 2001, ApJL, 548, L99
Zhou, Y., Feng, X., & Zhao, X. 2014, JGRA, 119, 9321
Zuccarello, F. P., Bemporad, A., Jacobs, C., et al. 2012, ApJ, 744, 66